



AFRL-RI-RS-TR-2019-025

QUANTUM INFORMATION SCIENCE

FEBRUARY 2019

FINAL TECHNICAL REPORT

APPROVED FOR PUBLIC RELEASE; DISTRIBUTION UNLIMITED

STINFO COPY

**AIR FORCE RESEARCH LABORATORY
INFORMATION DIRECTORATE**

NOTICE AND SIGNATURE PAGE

Using Government drawings, specifications, or other data included in this document for any purpose other than Government procurement does not in any way obligate the U.S. Government. The fact that the Government formulated or supplied the drawings, specifications, or other data does not license the holder or any other person or corporation; or convey any rights or permission to manufacture, use, or sell any patented invention that may relate to them.

This report was cleared for public release by the 88th ABW, Wright-Patterson AFB Public Affairs Office and is available to the general public, including foreign nationals. Copies may be obtained from the Defense Technical Information Center (DTIC) (<http://www.dtic.mil>).

AFRL-RI-RS-TR-2019-025 HAS BEEN REVIEWED AND IS APPROVED FOR PUBLICATION IN ACCORDANCE WITH ASSIGNED DISTRIBUTION STATEMENT.

FOR THE CHIEF ENGINEER:

/ S /

STEVEN T. JOHNS
Chief, Trusted Systems Branch
Computing & Communications Division

/ S /

GREGORY J. ZAGAR
Deputy Chief, Computing &
Communications Division
Information Directorate

This report is published in the interest of scientific and technical information exchange, and its publication does not constitute the Government's approval or disapproval of its ideas or findings.

REPORT DOCUMENTATION PAGE				Form Approved OMB No. 0704-0188	
<small>The public reporting burden for this collection of information is estimated to average 1 hour per response, including the time for reviewing instructions, searching existing data sources, gathering and maintaining the data needed, and completing and reviewing the collection of information. Send comments regarding this burden estimate or any other aspect of this collection of information, including suggestions for reducing this burden, to Department of Defense, Washington Headquarters Services, Directorate for Information Operations and Reports (0704-0188), 1215 Jefferson Davis Highway, Suite 1204, Arlington, VA 22202-4302. Respondents should be aware that notwithstanding any other provision of law, no person shall be subject to any penalty for failing to comply with a collection of information if it does not display a currently valid OMB control number. PLEASE DO NOT RETURN YOUR FORM TO THE ABOVE ADDRESS.</small>					
1. REPORT DATE (DD-MM-YYYY) FEBRUARY 2019		2. REPORT TYPE FINAL TECHNICAL REPORT		3. DATES COVERED (From - To) NOV 2015 – NOV 2018	
4. TITLE AND SUBTITLE QUANTUM INFORMATION SCIENCE				5a. CONTRACT NUMBER IN-HOUSE – R1YB	
				5b. GRANT NUMBER N/A	
				5c. PROGRAM ELEMENT NUMBER N/A	
6. AUTHOR(S) PAUL ALSING				5d. PROJECT NUMBER QCMP	
				5e. TASK NUMBER IN	
				5f. WORK UNIT NUMBER HO	
7. PERFORMING ORGANIZATION NAME(S) AND ADDRESS(ES) AFRL/RITA 525 Brooks Rd, Rome, NY 13441-4505				8. PERFORMING ORGANIZATION REPORT NUMBER	
9. SPONSORING/MONITORING AGENCY NAME(S) AND ADDRESS(ES) Air Force Research Laboratory/RITA 525 Brooks Road Rome NY 13441-4505				10. SPONSOR/MONITOR'S ACRONYM(S) AFRL/RI	
				11. SPONSOR/MONITOR'S REPORT NUMBER AFRL-RI-RS-TR-2019-025	
12. DISTRIBUTION AVAILABILITY STATEMENT Approved for Public Release; Distribution Unlimited. PA# 88ABW-2019-0425 Date Cleared: 31 Jan19					
13. SUPPLEMENTARY NOTES					
14. ABSTRACT This report discusses research conducted under the in-house AFRL/RI project Quantum Computing from FY16-FY18. In the sections below we discuss (i) the use of Aluminum Nitride (AlN) as a universal platform for quantum photonic integrated circuits (QPIC), (ii) theory and device characterization of a QPIC Quantum Photonic Processor (QPP), (iii) the important practical issue of Quantum Frequency Conversion, (iv) a Dual Mach Zehnder Interferometer capable of separating out the driving pump from the generated entangled photon pairs, (v) a detailed theoretical and experimental investigation of Spontaneous Parametric Down Conversion for entangled photon generation, (vi) a theoretical investigation of nonlinear optical processes in waveguide micro-ring resonators and (vii) an analysis of quantum algorithms conducted on the DWAVE quantum annealing machine.					
15. SUBJECT TERMS Quantum information processing, quantum entanglement, quantum computing					
16. SECURITY CLASSIFICATION OF:			17. LIMITATION OF ABSTRACT UU	18. NUMBER OF PAGES 64	19a. NAME OF RESPONSIBLE PERSON PAUL M. ALSING
a. REPORT U	b. ABSTRACT U	c. THIS PAGE U			19b. TELEPHONE NUMBER (Include area code) N/A

TABLE OF CONTENTS

LIST OF FIGURES	ii
LIST OF TABLES	iii
1.0 SUMMARY	1
2.0 INTRODUCTION	1
3.0 METHODS, ASSUMPTIONS AND PROCEDURES	3
3.1 Aluminum Nitride (AlN) as a universal platform for quantum photonic integrated circuits (QPIC)	3
3.2 A Quantum Photonic Processor (QPP): theory	4
3.3 Quantum Frequency Conversion: theory	6
3.4 A Dual Mach Zehnder Interferometer: theory	7
3.5 Analysis of Spontaneous Parametric Down Conversion (SPDC): theory	9
3.6 Nonlinear optical processes in micro-ring resonators (MRR): theory	14
3.7 Analysis of Quantum Algorithms for the DWAVE: background and theory	20
4.0 RESULTS AND DISCUSSION	22
4.1 Aluminum Nitride (AlN) quantum circuits: fabrication and experiments	22
4.2 A Quantum Photonic Processor (QPP): experiments	29
4.3 Quantum Frequency Conversion: experiments	31
4.4 A Dual Mach Zehnder Interferometer: fabrication and experiments	32
4.5 Analysis of Spontaneous Parametric Down Conversion (SPDC): experiments	34
4.6 Nonlinear optical processes in micro-ring resonators (MRR): results	38
4.7 Analysis of Quantum Algorithms for the DWAVE: assessment	41
5.0 CONCLUSIONS	43
6.0 REFERENCES	47
7.0 LIST OF SYMBOLS, ABBREVIATIONS, AND ACRONYMS	55

LIST OF FIGURES

Figure 1: Properties of AlN on sapphire material	3
Figure 2: Quantum Photonics Processor	5
Figure 3: Spontaneous four-wave mixing (SFWM) energy diagram	7
Figure 4: Comparison of ring resonator designs	8
Figure 5: Plot of SPDC intensity vs length with (green) and without (blue) Periodic poling.....	13
Figure 6: Single bus micro-ring resonator (MRR)	16
Figure 7: High cavity Q limit of a MRR	17
Figure 8: Hong-Ou-Mandel interferometer single SPDC source.....	17
Figure 9: Hong-Ou-Mandel Interference effect in MRR	18
Figure 10: Entangled biphoton generation (SPDC and SFWM) inside a MRR.....	19
Figure 11: Commutators for quantum noise operators inside a MRR	19
Figure 12: Reduced density matrix for the biphoton output state within a MRR	20
Figure 13: The exact values for the size of a minimum vertex cover in (d, n)	21
Figure 14: The QUBO formula for the vertex cover problem	21
Figure 15 Pseudocode to generate Vertex Cover QUBO coefficients	22
Figure 16: Fabrication of the AlN material platform.....	23
Figure 17: Coupling methods for the AlN waveguides	25
Figure 18: Resonances from the AlN micro-ring resonators	26
Figure 19: DBR and directional coupler in AlN	28
Figure 20: Fabricated dual MZI ring resonator.....	32
Figure 21: Resonance spectra of fabricated resonator	33
Figure 22: Coincidence ratio of MZI ring	34
Figure 23: Diagram of efficiencies, losses, and generation rates in a generic SPDC experiment	35
Figure 24: Diagrams of type-0, type-II (single-mode), and type-I (free space) biphoton sources.....	36
Figure 25 Hong-Ou-Mandel Interference Manifolds in MRR including internal loss	39
Figure 26: In-house designed and AIM fabricated MRR to test HOMI-manifolds prediction.....	39
Figure 27: CAR and heralding efficiency rates inside the MRR	40
Figure 28: Biphoton production rate inside the MRR.....	41
Figure 29: Embedding characteristics of vertex cover being solved on de Bruijn graphs.....	42
Figure 30: Embedding of the Vertex Cover QUBO for graph $B(2,5)$	42
Figure 31: Comparison of D-Wave results found to literature optimal solutions	43

LIST OF TABLES

Table 1: Fabrication parameters for the AlN material platform	24
Table 2: AlN platform results in literature.....	44

1.0 SUMMARY

Experimental and theoretical investigations were conducted to advance quantum information processing and computation, with a specific focus on photon-based qubits (quantum bits). These investigations included the generation and characterization of sources of entangled photons, chip-based quantum information processing circuits in quantum photonic integrated (waveguide) circuits (QPIC) devices, theory, design, fabrication, and testing of devices based on micro-ring resonator (MRR) devices, study of nonlinear processes spontaneous parametric down conversion (SPDC) and spontaneous four wave mixing (SFWM) in QPICs, and an analysis of quantum algorithms in quantum annealing devices. While much of the device research was conducted at telecomm wavelengths (1550nm), a significant portion of device research investigated the wideband gap material of Aluminum Nitride (AlN) as a step towards a ‘universal photonic platform’ capable of supporting wavelengths from the UV (for coupling to ytterbium trapped ion qubits ^{171}Yb in the UV 369nm) all the way through telecomm frequencies for long distance communications. The thorny issue of frequency conversion was also investigated, from both the UV to telecomm as well as from the visible to telecomm, again with an emphasis on AlN. Innovative single and entangled photon sources and circuits were investigated, including a dual Mach Zehnder MRR configuration which allowed for the efficient separation of the driving pump from the generated signal-idler entangled biphotons. A detailed theoretical investigation was carried out for the nonlinear entangled pair production process of SPDC, and subsequent experiments conducted show very close agreement with predicted rates. This investigation was extended to photon production and manipulation in MRR, and an extension of the Hong-Ou-Mandel Interference (HOMI) effect was predicted for MRR that included a much wider manifold of solutions than the standard bulk optic implementation using a beam splitter (BS). Our quantum annealing algorithm research focused on an in-depth exploration of a variety of graph theory NP-Complete combinatorial optimization problems solved over the class of de Bruijn graphs including the maximum cut problem, vertex cover problem, graph partitioning problem, maximum clique problem, independent set problem graph coloring problem, clique cover, Hamilton cycle problem, Steiner tree, directed feedback vertex set, feedback edge set, and undirected feedback vertex set.

2.0 INTRODUCTION

This report discusses research conducted under the in-house AFRL/RI project Quantum Computing from FY16-FY18. In the sections below we discuss (i) the use of Aluminum Nitride (AlN) as a universal platform for quantum photonic integrated circuits (QPIC), (ii) theory and device characterization of a QPIC Quantum Photonic Processor (QPP), (iii) the important practical issue of Quantum Frequency Conversion, (iv) a Dual Mach Zehnder Interferometer capable of separating out the driving pump from the generated entangled photon pairs, (v) a detailed theoretical and experimental investigation of Spontaneous Parametric Down Conversion for entangled photon generation, (vi) a theoretical investigation of nonlinear optical processes in waveguide micro-ring resonators and (vii) an analysis of quantum algorithms conducted on the DWAVE quantum annealing machine.

Since one of the primary goals of this in-house research was to advance the use of Aluminum nitride (AlN) as a universal photonic platform for quantum information processing, computing and interface to other matter qubits over a wide frequency range, we present here of brief introduction to this versatile material. Aluminum nitride (AlN) is one of the widest bandgap (6.015 eV, ~205 nm) semiconductors with attractive electronic and photonic properties, including transparency into the ultraviolet (UV) regime (365 nm wavelength and shorter). This broad spectrum makes it attractive for applications including UV spectroscopy [Krischeck10, Soltani16], optical waveguides for modular quantum computing with atomic memories [Nemoto14, Pant17, Duan10, Togan10, Childress14], nonlinear photonics throughout the UV to infrared [Xiong12], and solar-blind communications [Soltani16]. Many atomic transitions are in the UV or visible (VIS) spectrum, including Ytterbium ions, Strontium ions, Barium ions, and nitrogen vacancy (NV) centers in diamond, which have important optical transitions at 369.5 nm, 422 nm, 650 nm, and 637 nm, respectively. Recent work demonstrates the utility of integrated optics to perform quantum coherent operations on the optical qubit transition of Sr 88 at 647 nm [Mehta16]; the UV transmission of AlN-on-sapphire would also enable Sr 88 initialization at 422 nm or driving the 369.5 nm wavelength of Yb 171. Autofluorescence of silicon nitride (SiN) presents a challenge for pumping the diamond NV center at 532 nm [Mouradian15]; this autofluorescence is greatly reduced in AlN-on-sapphire, opening the path to large-scale photonic integrated circuits for atom-like qubits in diamond.

Electro-optic modulation presents an important capability in many applications, such as architectures for modular quantum computing. AlN has a relatively large electro-optic coefficient, and fast electro-optic modulation (4.5 Gb/s) has been demonstrated with AlN's high c-axis electro-optic coefficient ($r_{33} = 1$ pm/V) using sputtered AlN [Xiong12a]. Piezo-electric actuation of photonic devices has also been shown with optomechanical resonators [Xiong12b] and can potentially achieve very high modulation depth [Fang94]. Lastly, AlN has a high second order nonlinear susceptibility $\chi^{(2)}$ (4.7 pm/V) [Pernice12, Fujii77], as well as a third order nonlinear susceptibility with Kerr coefficient comparable to that of SiN (the n_2 for TE-like mode in the (001) plane is estimated to be $(2.3 \text{ pm}) \times 10^{-15} \text{ (cm}^2/\text{W)}$ [Jung13]. These nonlinear properties allow for a number of nonlinear optical processes [Jung14, Guo16, Liu17], including second harmonic generation [Pernice12, Troha16], sum/difference frequency generation [Jung16], photon pair generation by spontaneous parametric down conversion (SPDC) [Guo17], and spontaneous four-wave mixing (SFWM) [Jung13, Liu16]. The combination of the large bandgap with these nonlinear and electro-optic properties make AlN a promising platform for quantum devices and for other high-performance optics applications.

3.0 METHODS, ASSUMPTIONS, AND PROCEDURES

3.1. Aluminum Nitride (AlN) as a universal platform for quantum photonic integrated circuits (QPIC)

There is a need for UV/VIS photonics platforms based on AlN grown by plasma vapor deposition of nanocolumns on a sapphire substrate. X-ray diffraction shows low defect densities compared to previously-used AlN on SiO₂ [Xiong12], which will reduce propagation loss. We demonstrate essential photonic devices including ring resonators, distributed Bragg reflectors, and directional couplers. We show ring resonators with high intrinsic quality factor (Q) in visible ($Q > 170k$, loss = 4.9 dB/cm at 638 nm) and record-high quality factor in UV ($Q > 20k$, loss = 75 dB/cm at 369.5 nm). We demonstrate both vertical and edge coupling and compare them with simulation results. While autofluorescence is a problem in materials such as SiN, we find it to be low in the AlN on sapphire platform.

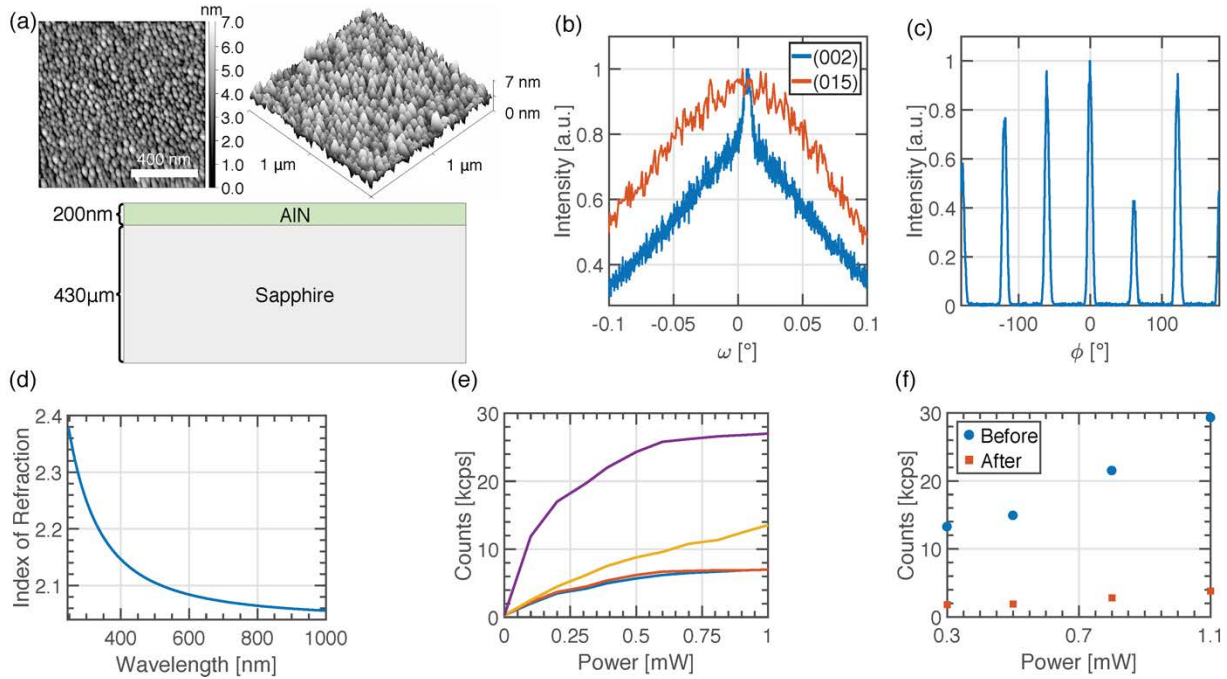


Figure 1. Properties of AlN on sapphire material.

Figure 1 shows the properties of AlN-on-sapphire material where; (a) Cross section illustrating each layer of the wafer, along with their respective thickness; top inset: atomic force microscopy scan of AlN film showing the nanocolumn size. Surface roughness is measured to be 0.9 nm RMS with 26.5 nm grain size (b) High resolution x-ray diffraction (002) and (015) omega scan of AlN. (c) (015) phi scan of AlN showing six-fold symmetry wurtzite structure. (d) Refractive index measurements using ellipsometry. (e) Background fluorescence from sapphire substrate (yellow), unpatterned AlN (blue), patterned AlN (orange), and stoichiometric silicon nitride (purple). (f) Background fluorescence from SiON top cladding, before (blue circles) and after (orange squares) bleaching. Figure1(a) illustrates the commercially available AlN-on-Sapphire wafers from Kyma

Technologies, Inc., consisting of 430 μm sapphire (Al_2O_3) with a 200 nm c-plane AlN film on the top layer, which is used for fabricating quantum photonic integrated circuits (QPICs) in this work. The c-plane AlN is grown on top of the sapphire substrate by pulsed DC magnetron sputtering, using a process called plasma vapor deposition of nanocolumns (PVDNC). This method produces an AlN thin film that is crystalline with the [0001] direction parallel to the growth direction. Atomic force microscopy of the AlN thin film shown in the inset of Fig. 1 (a) indicates a flat surface with 0.9 nm RMS roughness. High-resolution X-ray diffraction (HRXRD) measurements in Fig. 1 (b) indicate the high structural quality of the AlN thin film. The omega scan of (002) and (015) AlN peaks shows full-width-half-maximum (FWHM) of 0.12 degree and 0.20 degree respectively, which is 10 to 20 times smaller than the previous results of AlN thin films deposited on amorphous silica [Lin14]. The single crystalline wurtzite structure across the wafer is evidenced by the (015) phi scan showing six-fold symmetry (Fig. 1 (c)). This flat surface and improved structural quality likely contribute to the low waveguide loss described below. Figure 1 (d) plots the measured refractive index of the AlN film spanning from UV to VIS to near infrared wavelengths. The power dependence of this platform's background autofluorescence using $\lambda = 532$ nm excitation pump is shown in Fig. 1(e). For comparison, Fig. 1(e) also shows the autofluorescence results of a SiN sample under the same excitation and collection conditions. The SiN sample has close to four times the amount of fluorescence intensity as AlN; however, the amount of autofluorescence is dependent on the SiN composition and method of deposition [Moss13]. Furthermore, the photoluminescence (PL) from pumping the AlN is mainly from the underlying sapphire substrate. Spectrally, this sapphire fluorescence is concentrated in a narrow band sapphire Cr line at around 690 nm, which can be easily filtered out by a notch filter. This is more favorable for quantum applications compared to the broadband SiN PL from 620 nm to 800 nm, which overlaps spectrally to NV in diamond spectrum [Mouradian15]. A low autofluorescence makes AlN promising for interfacing with atomic transitions of ions [Monroe13], neutral atoms [Goban14], and atom-like defects in diamond [Mouradian15]. Initially after deposition, the SiON cladding (to be discussed later) exhibits some fluorescence comparable to SiN, but the fluorescence can be bleached away by optically pumping the material with the excitation laser, as shown in figure 1 (f).

These properties make AlN and its alloys an extremely exciting platform for the creation of photonic devices. The combination of the wide bandgap, the high nonlinearity, and the electro-optic coefficient allow for the creation of fast reconfigurable photonic circuits in which the qubits can be generated, manipulated, and frequency converted in a single platform. The next section will describe the fabrication of such devices in this platform and the experimental results.

3.2 A Quantum Photonic Processor (QPP): theory

Integrated optics represents the most promising avenue for the large scale development of practical (i.e. fieldable) quantum optics devices. The advantages in size weight and power (SWAP) are enormous and as such it is a rapidly developing field. The most advanced area uses telecom wavelengths and devices built in the silicon on insulator (SOI) platform which is a CMOS

compatible system. Indeed the base wafers used can be identical. One of the goals of this field is to create a large and arbitrary transformation.

The Quantum Photonic Processor (see Fig. 2) is a large (1cm by 2cm) integrated optical device containing 88 Mach-Zender Interferometers (MZI). Each MZI is a 2 mode mixing device that can be thought of as a variable beam splitter. These 88 MZIs are arrayed with overlapping nearest neighbor design between 26 input and output modes. This creates a triangular structure seen below.

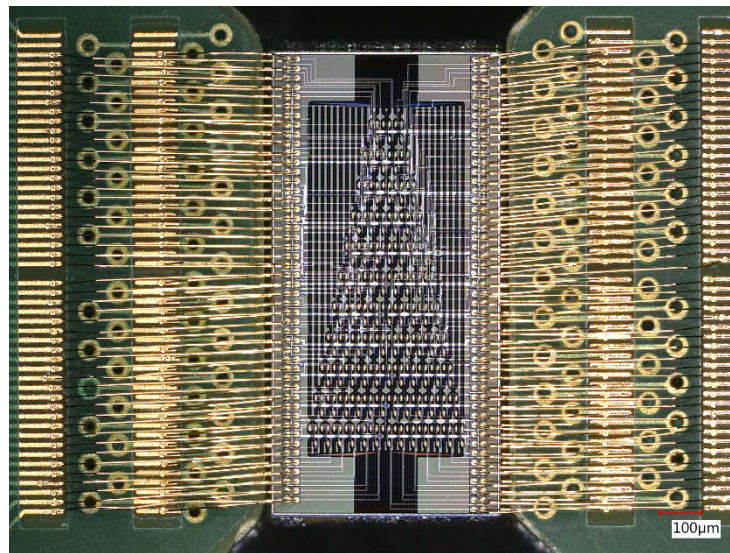


Figure 2. Quantum Photonics Processor

This device was designed in collaboration with MIT and the group of D. Englund, it has been used for several experiments including tests of Anderson localization, ballistic transport and boson sampling [Harris15]

Under this project we have developed a numerical simulator for single photon operation of the MZI array, as well as a calibration method for the full device. In addition we have worked with our collaborators to transfer their efforts and results to the in house AFRL quantum optics lab.

A second generation device has been designed based on the performance and use of the QPP. This work was performed with RIT and the group of S. Preble. The second generation device can perform an arbitrary 3 qubit transformation which is larger than the current QPP. This device was designed in house and fabricated by AIM photonic. AIM photonic is a government supported CMOS foundry started in upstate NY with the goal of developing next generation technology and helping commercialize them. The devices have been fabricated and delivered to AFRLs in house quantum lab and undergone preliminary testing.

3.3 Quantum Frequency Conversion: theory

Quantum frequency conversion has the goal of changing the wavelength of a single photon. Frequency conversion of classical lasers in nonlinear crystals is a well known practice for certain wavelengths via processes such as Sum Frequency Generation (SFG), Difference Frequency Generation (DFG) and Second Harmonic Generation (SHG). These processes use various combinations of signal and pump beams and the second or third order nonlinearity of a crystal to convert one frequency to another. This process is required to convert the output of the qubits to telecom.

Work under this project focused on DFG between the 369.5nm output of trapped Ytterbium ions and telecom (~1550nm). With DFG there are two options, bulk phase matching or quasi-phase matching. Quasi-phase matching in waveguides gives the highest conversion efficiency due to the waveguide confinement (higher intensity) and longer available interaction length. Quasi-phase matching is based on creating a periodically poled crystal in which the crystal dipole is reversed periodically such that the phase matching (momentum) is preserved such as periodically poled lithium niobate (PPLN).

In collaboration with the group of A. Sergeenko and Boston University numerical tests were performed to find the correct polling period. This depends on the material characteristics of the chosen crystal, lithium niobate (LiNbO₃) and the pump and target wavelengths. Given a seed of 369.5nm, a target of telecom (~1550nm) and the characteristics of LiNbO₃ the ideal polling period of the crystal is 2.34μm with a pump wavelength of 483nm. The wavelength of the pump is set by simple conservation of energy. In DFG one signal photon and one pump photon turn in to two pump photons an extra photon with energy equal to the different of the signal and pump. The Polling period represents a significant challenge for the state of the art in fabrication. Most PPLN devices operate at wavelengths that require 6-40μm polling periods. The smaller the polling period the more difficult it is to produce as the lithography techniques required become more of a challenge.

An alternative that was studied is a two stage conversion process suggested by several groups [Pelc12, Kim13]. Instead of a direct transmission an intermediate step is used along with two crystals at different polling lengths and two pump lasers are used. This can have several advantages including lower noise due to unwanted processes [Pelc12, Kim13]. We examined and obtained crystals capable of such a two stage process but our analysis of alternatives concluded that the added difficulty, size weight and power (SWAP) requirements, laser requirements, and the cost in efficiency was not worth the minor improvements in areas such as single to noise ratio.

3.4 A Dual Mach Zehnder Interferometer: theory

With the capability of integrating hundreds of optical components into a single photonic chip, there is an added benefit of maintaining phase stability between the integrated optical components. In turn, large-scale processing of optical information reached a point previously thought to be unachievable. The bottle-neck of single-photon processing is then pushed to the generation of many identical single-photons. A reasonable approach towards many single photon sources is recruit integrated optics for generation.

Silicon-on-insulator (SOI) is a mature process which leverages many of the same techniques used in computer chip fabrication. SOI as a technology is not without draw-backs and for single-photon generation, there are compromises to be made. Arguably the most significant is that, there is no second-order nonlinearity in the silicon which comprises the core of the optical waveguides. In turn, single-photons must be generated via the third-order nonlinear process of spontaneous four-wave mixing (SFWM.) This process is schematically represented in the Fig. 3 below where two pump photons (green) generate a pair of photons (red and green.) The generated photons satisfy energy conservation and momentum conservation of the pump photons.

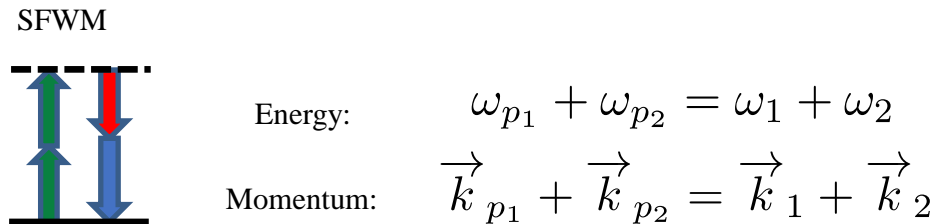


Figure 3. Spontaneous four-wave mixing (SFWM) energy diagram

Even though silicon has a relatively high nonlinearity, the magnitude of this third-order effect is small. Therefore, to ensure reasonable photon generation probability we must utilize resonant enhancement of the optical fields on the device. We achieve this effect by using ring resonators. Such devices can lead to over a 100-fold enhancement of the optical fields, while also enforcing a spectrum of the photons generated (i.e. the spectrum of the resonances.) For a more detailed depiction of the behavior of ring resonators, refer to Section 3.6. Generally, resonance happens when photons which make a round trip inside the ring destructively interfere with photons attempting to pass the ring. Balancing the round-trip loss to the input coupling strength of photons at these wavelengths of interference (resonances) leads to a perfect destructive interference so no photons on resonance make it past the ring – they all couple into the resonator until lost by other means. This perfect balancing of round-trip loss to pass-by coupling is known as critical coupling and it leads to the largest resonant enhancement inside the ring. Coupling more or less light than

is lost in a round trip leads to over- and under-coupling, respectively. These conditions lead to a lower depth of the resonance and for greater over-coupling, there is a broader resonance spectrum for a given resonance.

If all that we were concerned with was photon generation rates, then just using a simple resonator would be enough to get a single-photon source. Since we intend on using multiple sources on chip and interfering their generated photons, we need to also ensure that the photons can properly interfere with each other. Therefore, we should make careful considerations about the resonator's spectrum.

Spectral overlap between two resonators can be achieved by tuning the resonator sizes with the thermo-optic effect. Having the same spectral profile of the resonators gets us half-way there. The photons that are generated in the process of spontaneous four-wave mixing are a consequence of energy and momentum conservation. Thanks to the identical coupling for the pump photons and the generated photons, there are more ways to conserve photon energy of the pump than there are ways that the pump can be described. In turn, photons generated by identical coupling to a resonator will contain spectral correlations that are great enough for the photons to share entanglement in their energy. One must decouple the relationship between pump wavelength resonances and generated photon resonances.

In addition to decoupling the wavelength resonances between pump and signal photons, we also have a desire to separate the pump photons from the signal photons. We note that there are two main ring resonator designs. First, the single bus resonator (see Fig. 4) which has a single

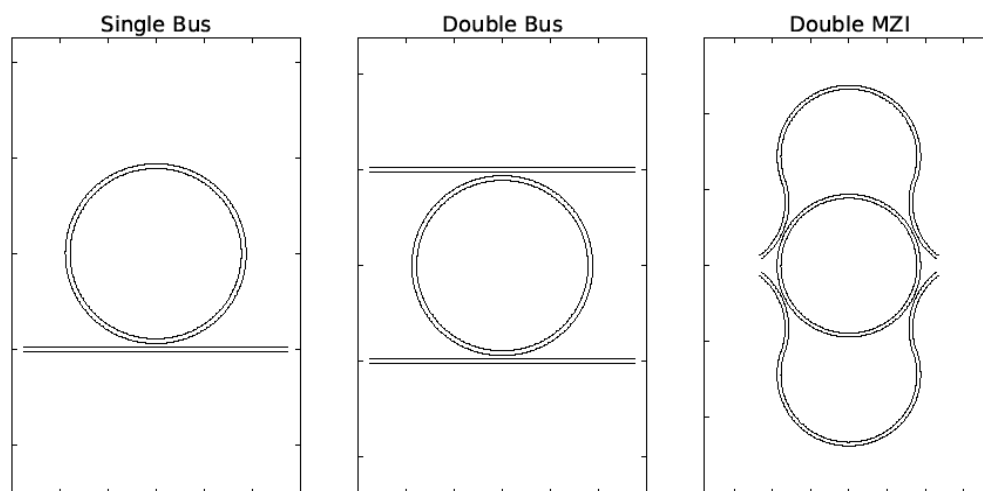


Figure 4. Comparison of ring resonator designs.

waveguide coupled the ring. This configuration has the greatest interaction strength since the round-trip loss is limited to only the waveguide loss. The downside of a single bus ring is that the

pump wavelengths share the same output waveguide as the photons generated by the ring and can lead to further complications later in the optical circuit. If we move to a double bus resonator (i.e. two waveguides coupled to the resonator), we allow for light to coupling out of the ring within its round-trip. Therefore, we effectively increase the round-trip loss of the ring. Although by introducing additional loss we have lowered the ring's resonant enhancement, the second bus allows collection of signal photons while reducing the amount of pump photons coupled into the single photon waveguide.

Our approach alleviates the issues of single and double bus ring resonators by relying on interferometric coupling to the ring resonator. For instance, by utilizing a Mach-Zehnder interferometer (MZI), one has access to a tunable waveguide coupler (e.g. directional coupler) which, as a function of relative path length, leads to a sinusoidal behavior in transmission with change in relative path length. Choosing a relative path length that is a harmonic away for a wavelength λ leads to the same operation of the MZI for wavelengths near λ and quickly changes behavior as the input wavelength is changed. In other words, the MZI becomes wavelength dependent. In fact, the MZI transmission is sinusoidal in the input wavelength and the period of its oscillation depends on the order of the harmonic chosen. For our purposes, we choose the relative path length to be $dL = (\lambda^2 - \delta\lambda^2)/(2n_g\delta\lambda)$ for group index n_g , chosen wavelength λ and period of oscillation $\delta\lambda$. Considering the free spectral range of a ring resonator δL corresponds to a round trip length of $2dL$, we detune two such MZI couplers such that they alternate in maximal transmission (i.e. high transmission for one MZI at a wavelength corresponds to low transmission for the other MZI) leading to an effective single bus ring resonator for each MZI where the free spectral range is twice that of the underlying ring resonator. These structures are given by the figure above where a single bus ring resonator has only a single coupling to the ring, the double bus resonator has two couplings and the double MZI coupled ring has two interferometric couplers.

The double MZI ring has the ability of having two different coupling strengths. The sets of coupling strengths correspond to the maximal transmission of the top (bottom) MZI section while observing maximal reflection from the bottom (top) MZI section. In turn, by over-coupling the pump wavelength and critically coupling the generated photons a resonance out, we remove the entanglement in frequency between the generated photons. Conversely, over-coupling the generated photons and critically coupling the pump photons leads to a bright source with a very high probability of collecting the photons generated inside of the ring.

3.5 Analysis of Spontaneous Parametric Down Conversion (SPDC): theory

In order to have a solid framework to understand and perfect sources of both heralded single photons and entangled photon pairs generated in SPDC, it is necessary to be able to predict the quantitative as well as qualitative properties of the light generated in this way. To accomplish this, as well as opening up the quantum optics of entangled photon pairs to a wider audience of physicists and engineers, we authored a comprehensive tutorial [Schneeloch18] where the absolute brightness and other properties of entangled photon pairs are calculated from first principles, with

all necessary assumptions and approximations discussed in detail. Most importantly, we test the success of our theoretical predictions with experimental data from a variety of sources, showing good agreement. While most experimental sources of entangled photon pairs fall under the same classes of approximations and assumptions, clearly delineating them allows us to understand the limits of our theoretical understanding, and to consider whether non-standard designs might actually offer superior performance. On top of this, having access to a single, comprehensive, unified reference instead of needing a large collection of differently written research articles will greatly increase the accessibility of nonlinear quantum optics to new graduate students, while increasing the visibility of the research contained in these important articles.

In our theoretical study, we first derive the absolute photon-pair generation rate in SPDC for a broad swath of experimental setups and parameters including: types 0, I, and II phase matching, for both degenerate and non-degenerate frequencies, for both ordinary, and periodically poled nonlinear crystals, with both appreciable and negligible group velocity dispersion, and for light coupled into both single-mode optical fiber and into free space. On top of this, we also discuss the photon number statistics of the SPDC light, show the origin of Optical Parametric Oscillation, discuss the fundamental tradeoff between heralding efficiency and absolute efficiency of photon pair generation, and finally, and discuss the effects on SPDC when the nonlinear medium is placed in a cavity near resonance with the pump. As mentioned previously, we also test the validity of our formulas with three different experimental demonstrations (discussed in Section 4.5). As an unanticipated side benefit, much of the theoretical framework discussed here for SPDC also works

well toward treating another nonlinear-optical source of entangled photon pairs: Spontaneous Four-Wave Mixing (SFWM). Both SPDC and SFWM are mechanisms amenable to adaptation toward integrated (i.e., on-chip) sources of entangled photon pairs, indistinguishable photons for optical quantum computing, and heralded single photons in applied quantum information science (QIS).

In order to obtain our results, we had to calculate the quantum state of the biphotons produced in SPDC. Because most experimental sources of entangled photon pairs have absolute conversion efficiencies of 10^{-8} to 10^{-12} , the probability is low enough that we successfully apply first-order time-dependent perturbation theory to solve the Schrödinger equation for the quantum electromagnetic field. To do this, we also discussed what in nonlinear optics contributes to the precise Hamiltonian for the electromagnetic field, on which the Schrodinger equation relies. Where the initial state of the field is a coherent state at the pump frequency, and is a vacuum state at all other frequencies outside the pump bandwidth, we find the state of the biphoton as the state of the field after the laser has interacted with the nonlinear crystal for amount time T_{DC} . Here, T_{DC} is the down-conversion time, or the time it takes a pump photon to travel the length of the nonlinear medium. While this time is of the order picoseconds for millimeter-scale crystals, this state represents picoseconds worth of biphotons generated as the pump photons exit the crystal, and new pump light enters. From this state, we calculate the probability of biphoton generation in time

T_{DC} , and because this is also a Poisson point process, we get the mean number of biphotons generated per unit time by dividing this probability by the time T_{DC} .

While the previous description makes it seem like a single calculation or formula describes the brightness of all SPDC experiments, the previous calculations only form a framework to describe the brightness, while the exact dependence can vary greatly between different experiments. The biphoton state $|\psi\rangle_{SPDC}$ can be discussed in terms of five parts. The first two parts are the nonlinear optical susceptibility and pump amplitude, whose effect on the brightness of SPDC is constant across all implementations. The remaining three parts can differ significantly between experiments: the energy conservation; the mode overlap; and the phase matching:

$$|\psi\rangle_{SPDC} \cong \sum_{\vec{\mu}_p, \vec{\mu}_1, \vec{\mu}_2} \sqrt{\frac{2\hbar\omega_p\omega_1\omega_2 d_{eff}^2}{\epsilon_0 n_p^2 n_1^2 n_2^2 L_z^2}} \underbrace{\left(\int dx dy g_{\vec{\mu}_p}^*(x, y) g_{\vec{\mu}_1}(x, y) g_{\vec{\mu}_2}(x, y) \right)}_{\text{Mode overlap}} \underbrace{\left(\int dz \tilde{\chi}_{eff}^{(2)}(z) e^{-i\Delta k_z z} \right)}_{\text{Phase matching}} \underbrace{\left(\int_0^T dt' e^{i\Delta\omega t'} \right)}_{\text{Energy Conservation}} \alpha_{k_p, \vec{\mu}_p} \hat{a}_{\vec{\mu}_1, k_1}^\dagger \hat{a}_{\vec{\mu}_2, k_2}^\dagger |0, 0\rangle \quad (1)$$

Here, the spatial integrals are taken over the volume of the nonlinear medium, or if the mode functions $g_{\vec{\mu}}(x, y)$ are approximately confined to within the medium, then over all space. The effective second-order optical nonlinearity d_{eff} is the first factor determining the likelihood of SPDC. In materials with centrosymmetry, either by a centrosymmetric crystal structure, or an isotropic medium (e.g., liquids, gases, and glasses), d_{eff} will be zero, and SPDC will not be possible.

The first striking thing about the state of the biphoton is that non-energy-conserving transitions are possible. However, even over the time scales of T_{DC} energy conservation is nearly assured because the biphoton state at time T_{DC} requires integrating the phase $e^{i\Delta\omega t}$ from time 0 to T_{DC} . Here $\Delta\omega$ is equal to the difference between the energy (not counting Planck's constant) of the created photon pair and the annihilated pump photon. When $\Delta\omega$ is much larger than $1/T_{DC}$, the phase is rapidly oscillating, and the corresponding amplitude from integration washes out to a value tending towards zero.

The mode overlap is the first aspect of the biphoton state we have significant control over. First, we have freedom over the choice of the basis of mode functions $g_{\vec{\mu}}(x, y)$ that we use, which may be adapted to fit a particular experiment. For coupling entangled photon pairs into single-mode optical fiber, the optimum basis would be either the Hermite-Gaussian, or Laguerre-Gaussian basis, with parameters selected to correspond to the mode field diameter of the optical fiber. Alternatively, a custom basis of spatial modes can be constructed to fit an experimental single-mode waveguide formed by processes that produce asymmetrically shaped modes. In addition, certain bases of spatial modes carry additional physical significance; there is a subset of Laguerre-Gaussian modes that are eigenmodes of the Orbital Angular Momentum (OAM) of light, and are called OAM modes for short.

The third, and perhaps most discussed determination of the quality of down-converted light is the phase matching function (PMF). Where the energy conservation is approximately assured due to a rapidly oscillating phase of $e^{i\Delta\omega t}$, momentum conservation is correspondingly assured due to the rapidly oscillating phase of $e^{-i\Delta k_z z}$. What makes the phase matching function more involved is that the momentum k_z (omitting Planck's constant) is dependent on optical dispersion, or how the index of refraction changes with frequency. In particular, where $k_z c = \omega n$, and n is the refractive index at frequency ω :

$$\Delta k_z = \frac{\omega_1 n(\omega_1)}{c} + \frac{\omega_2 n(\omega_2)}{c} - \frac{\omega_p n(\omega_p)}{c}. \quad (2)$$

Because of this, we obtain a plethora of different formulas and qualitative relations depending on whether or not the frequencies are degenerate; whether or not the polarizations of the biphoton are identical, and whether or not the dispersion is so small that we have to go to multiple orders in frequency to adequately describe it. For example, the formula for type-1 degenerate SPDC with a collimated Gaussian pump beam of power P , standard deviation σ_p , and frequency ω_p , incident on nonlinear crystal of length L_z , nonlinear susceptibility d_{eff} , and group velocity dispersion κ_1 into a single Gaussian spatial mode of standard deviation σ_1 is given by the rate R_{SM} :

$$R_{SM}^{type-I} = \sqrt{\frac{2}{\pi^3}} \frac{2}{\epsilon_0 c^3} \frac{n_{g1} n_{g2}}{n_1^2 n_2^2 n_p} \frac{d_{eff}^2 \omega_p^2}{\sqrt{\kappa}} \left| \frac{\sigma_p^2}{\sigma_1^2 + 2\sigma_p^2} \right|^2 \frac{P}{\sigma_p^2} L_z^{3/2} \quad (3)$$

where n_{g1}, n_{g2} are the group indices of refraction at the signal and idler frequencies, and n_1, n_2, n_p are the (standard) indices of refraction at the signal, idler, and pump frequencies, respectively. The corresponding formula for the identical parameters, but involving type-II SPDC would be:

$$R_{SM}^{type-II} = \frac{1}{\pi \epsilon_0 c^2} \frac{n_{g1} n_{g2}}{n_1^2 n_2^2 n_p} \frac{d_{eff}^2 \omega_p^2}{|n_{g1} - n_{g2}|} \left| \frac{\sigma_p^2}{\sigma_1^2 + 2\sigma_p^2} \right|^2 \frac{P}{\sigma_p^2} L_z \quad (4)$$

These different types of degenerate SPDC scale differently with length because in type-II SPDC, $n_{g1} \neq n_{g2}$ at the same frequency due to the polarizations of the signal and idler light being mutually orthogonal and the medium being birefringent. Because of this, when we integrate over the signal and idler momenta to get these total rates, we only need to express Δk_z to first order in ω , while for type-I degenerate SPDC, we need to expand Δk_z out to second order since the linear term dependent on $n_{g1} - n_{g2}$ would equal zero.

On top of this, it may be the case that the indices of refraction are such that Δk_z is far enough away from zero that SPDC is not experimentally possible in a given material at a given frequency band. In these cases, we can consider periodically poling the medium, or flipping the crystal axis back and forth over its length, or mathematically, flipping $\bar{\chi}_{eff}^{(2)}(z)$ from 1 to -1 and back. This flips the oscillation of $e^{-i\Delta k_z z}$ so that just as it reaches a maximum, it becomes a minimum again, and continues to increase with z instead of returning to zero (See figure 5). With periodic poling, we

can compensate for otherwise unfavorable dispersion in a nonlinear medium with other desirable properties.

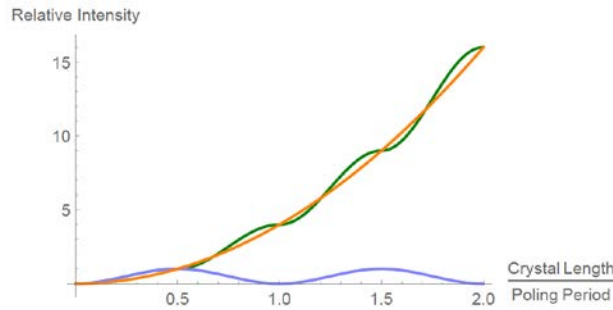


Figure 5. Plot of SPDC intensity vs length with (green) and without (blue) Periodic poling.

On top of these useful formulas for the brightness of photon pairs in diverse implementations of SPDC, we also consider the regime where the pump power may be so bright (e.g., with a pulsed pump of short duration) that first-order perturbation theory may no longer be valid. With the framework already laid out, we instead solve to find the full biphoton field state in a different approximation. When the pump is narrowband enough to be approximated as monochromatic, and bright enough that the loss of single photons is insignificant, we can instead solve the (Heisenberg) equations of motion for the creation operators of the field to find the number statistics of the down-converted light beyond the regime where the field may only produce either zero or one photon pair by time T_{DC} . In doing so, we see an exponential gain in photon pair brightness for sufficiently bright pump powers and long enough interaction times, which reproduces the linear dependence in the low-pump-power limit. The resulting quantum state of the field is a multi-mode-squeezed vacuum state, composed of products of two-mode-squeezed vacuum states for each correlated pair of momentum modes of the field. When this exponential gain exceeds the exponential loss due to absorption, scattering, etc, this is known as the threshold for Optical Parametric Oscillation (OPO). It is a common strategy to use OPO in an optical cavity as a source of squeezed light. The threshold for OPO is distinct from the scale of pump powers necessary to be outside the scope of first-order perturbation theory. Where this scale of pump power is well over 1 MW for typical experiments, this regime is only approached with pulsed pump lasers with a moderate mean power, but a very short pulse duration. In this regime, the probability of generating multiple biphotons over time T_{DC} is significant enough to affect heralding efficiency and experimental data.

In a regime where the efficiency is high enough that significant pump depletion is possible, we also examined how the field evolves in time outside of the undepleted pump approximation, though for simplicity, only for a single correlated pair of down-converted modes coupled to the pump mode. In this approximation, the equation of motion for the down-converted mode operators can be solved using techniques similar to the nonlinear pendulum. Like a pendulum, we see that the amplitude of the down-converted light oscillates between zero and a maximum value, at which point, the reverse processes to SPDC known as Second Harmonic Generation (SHG) and Sum Frequency Generation (SFG) become more efficient.

As will be discussed in section 3.6, we have also examined the effect of cavity enhancement in the efficiency of nonlinear optics, and the properties of the down-converted light created where the nonlinear medium is structured as a micro-ring resonator (MRR). Because of this, we were able to show a similar tradeoff between heralding efficiency and absolute brightness afforded by cavity enhancement. However, even though there is loss over multiple round trips, the fraction of photon pairs that successfully couple out of the resonator is not rendered insignificant, but remains appreciable near critical coupling.

In this study, we come to appreciate the full scope of the challenge of creating an ideal heralded single photon source, and also find that the theoretical tools of quantum optics are adequate for more than a qualitative description of the behavior of SPDC in realistic experiments. With this research constituting a solid understanding of the physics of Photon pair generation in SPDC, we are moving forward in multiple avenues finding techniques in integrated optics to produce a high heralding efficiency while maintaining a large enough flux of heralded single photons to be applied in integrated photonic processing.

3.6 Nonlinear optical processes in micro-ring resonators (MRR): theory

It is difficult to overstate the importance of the control of fields at the single or few photon level in the realization of optical architectures for quantum computation, communication, and metrology. In order to optimize the functionality of next-generation quantum information processing systems, devices need to be scaled to the level of micro- or even nano-integration. Notable persistent challenges to advancement of efficient, scalable quantum information processing systems include the identification of useful physical qubits, the discovery of materials for use in quantum circuits, and the development of system architectures based on those qubits and materials. Light-speed transmission and high resilience to noise in comparison with other possible physical systems identifies photons as a very promising realization of the carriers of quantum (and classical) information. Further, several degrees of freedom, for example, presence/absence of a photon or mutually orthogonal optical polarization states can be used to encode quantum information.

One potential platform is silicon, which has desirable optical properties for integrated optical systems at the telecommunication wavelength of 1550 nm. In addition, silicon is a candidate for fabricating sub-Poissonian single photon sources relying on its high third order nonlinearity χ^3 . Using such sources, several diverse and exciting quantum phenomena can be explored, including time bin entanglement, polarization entanglement, and N00N reduced de-Broglie wavelength. Pioneered largely by the early work of Yariv [Yariv00, Yariv02], silicon micro-ring resonators (MRR) evanescently coupled to silicon wave guides find an ever-growing range of applications as the bases for devices and networks that are at the heart of the phenomena underpinning many quantum technologies.

In the following, we discuss the theoretical research we have conducted towards engineering quantum photonic devices with MRR, and our efforts towards experiments with such devices. In

particular, in collaboration with researchers at the Rochester Institute of Technology we have recently demonstrated theoretically a particular enhancement of the Hong-Ou-Mandel Effect [Hach:2014] and experimentally a two-photon interference effect in down converted photons generated on-chip in a silicon micro-ring resonator. Naturally paralleling the increased interest in silicon micro-ring resonator networks, a significant body of theoretical analysis has developed into a reasonably sophisticated description of the quantum optical transport behaviors exhibited in various simple topologies and environments. Two basic approaches have emerged in formulating the theoretical description of such systems. One that we shall refer to as the Langevin approach is based upon Lipmann-Schwinger style scattering theory at the localized couplers between components (i.e. micro-rings and waveguides) along with photonic losses modeled via noise operators representing a thermal bath of oscillators. The second approach, which we describe below, which we will loosely call "operator valued phasor addition" or the OVPA approach, is based upon the construction of field transformations for the optical mode operators by considering a linear superposition of transition amplitudes through all possible paths of the optical system.

We also discuss our investigation into entangled photon pair generation in a micro-ring resonator using our input-output formalism discussed above based on the work of both [Raymer-McKinstrie13] and [Alsing-Hach17a] that incorporates the circulation factors that account for the multiple round trips of the fields within the cavity. We considered biphoton pair generation within the MRR via both SPDC and SFWM, and compute the generated two-photon signal-idler intra-cavity and output state from a single bus (all-through) micro-ring resonator. We also compute the two-photon generation, coincidence-to-accidental and heralding efficiency rates. We compared our results to related calculations in the literature obtained using the standard Langevin input-output formalism.

Quantum Optics in Micro-ring Resonators

Fig. 6 illustrates several approaches that have been used in the literature to analyze the quantum optics inside a micro-ring resonator (MRR). In the upper left hand corner is the standard Langevin approach found in the textbook of Wall and Milburn [Walls94] which relates the single mode internal field a_{int} of the MRR to the external driving field a_{out} , where γ_c and γ_{int} represent the losses due to the (leaky) cavity mirror(s) and the internal (scattering) losses, respectively.

A close examination of this standard Langevin approach shows that it is strictly valid only near mmr resonances, i.e. when round trip (accumulated) phase θ of the MRR is a multiple of 2π , where the intensity internal field is strongest. In order to obtain expressions for the internal field for all values of θ (i.e. both on and off resonances, throughout the MRR's free spectral range) Raymer

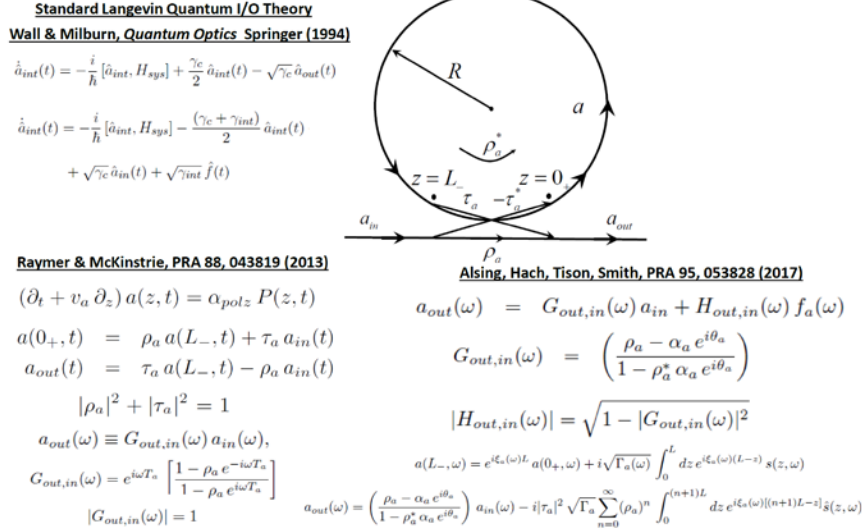


Figure 6. Single bus micro-ring resonator (MRR)

and McKinstrie [Raymer-McKinstrie13] adopted a beam splitter (BS) approach (lower left hand corner of Fig. 6) to the case of a internally lossless MRR, taking only into account the losses of the field at the cavity mirrors. Here τ_a and ρ_a are the MRR transmission (between the waveguide bus and the ring cavity) and reflection (bus to bus, or within the ring cavity) coefficients, respectively. This leads to a (unitary) transfer function $G_{in,out}(\omega)$ that allows one to describe the ring output field (just exiting the MRR) a_{out} to the external input field a_{in} (just entering the MRR), $a_{out}(\omega) = G_{in,out}(\omega) a_{in}(\omega)$. Alsing and Hach [Alsing-Hach17a] extended this derivation to included internal scattering losses, while directly taking into account the all roundtrip passages of the internal field, as shown in the lower right hand corner of Fig.1. The inclusion of internal losses leads to the formula $a_{out}(\omega) = G_{in,out}(\omega) a_{in}(\omega) + H_{in,out}(\omega) f_a(\omega)$, where $f_a(\omega)$ are the quantum noise operators needed to maintain unitarity when losses are included (in the Heisenberg picture) and $H_{in,out}(\omega)$ represents the transfer function of the internal field into quantum noise when photons are lost through internal scattering. This internal scattering loss is characterized by the parameter $0 \leq \alpha_a \leq 1$, which also shows up in a semiclassical formulation [Yariv00, Yariv02] where the quantum (operator) noise $H_{in,out}(\omega) f_a(\omega)$ is neglected. To show that their formulations agreed with that of Raymer and McKinstrie and also with the standard Langevin approach, Alsing and Hach compared their formulation in the high cavity Q limit (see Fig. 7) in which (small) mirror losses and internal loss are expanded as exponentials with small arguments. This leads to standard expressions for both $G_{in,out}(\omega)$ and $H_{in,out}(\omega)$ as derived by the usual Langevin methods (both classical and quantum) as shown in Fig. 7.

Hong-Ou-Mandel Manifolds

As an application of the above MRR formulation, Alsing and Hach considered the Hong-Ou-Mandel Interference (HOMI) effect inside a MRR. In standard bulk optics approaches, this is

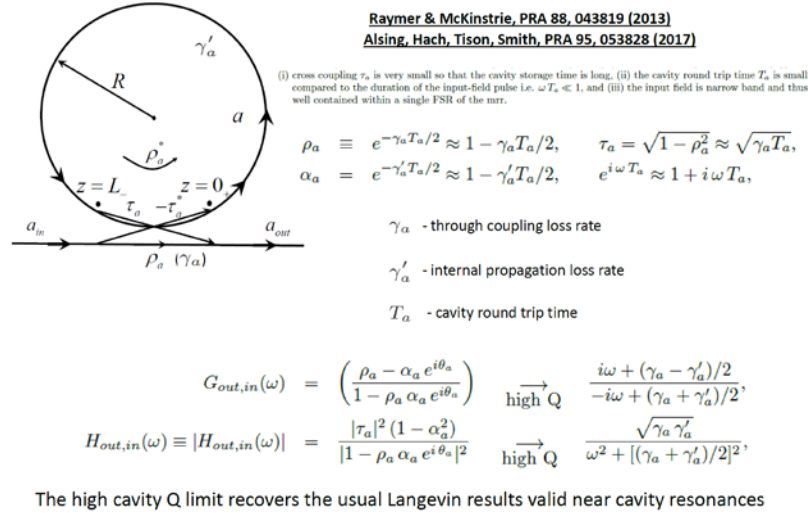
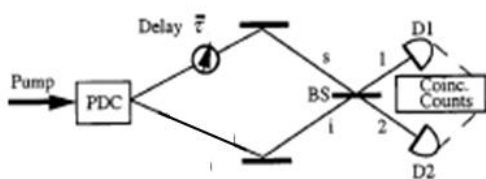


Figure 7. High cavity Q limit of a MRR.

usually performed by interfering the signal and idler output of entangled biphoton (from a spontaneously parametric down conversion (SPDC) source) on a BS. The HOMI effect is a standard tool to access the indistinguishability quality of a biphoton source leading to an 100% interference dip (0 coincidence counts) upon complete destructive interference (which sends both photons to either one of two detectors).

In an application of photon entanglement it is essential to designate which photon properties (momentum, energy (spectral), polarization, spatial, or temporal etc.) in a given configuration are to be entangled, and to ensure that no others yield information to degrade the desired quality of interference. Quantum interference relies on indistinguishable amplitudes (“Feynman paths”) leading to an event. In this case will be photon pair detection in coincidence counting modules. To illustrate consider first the HOMI (Fig. 8) where two photons meet at a beam splitter (BS). If



Consider amplitudes that yield coincidence counts in the single photon counting detectors (D1,D2); where the events are: a photon with frequency ω_1 in D1 , and a photon with frequency ω_2 in D2 .

Two paths to this event via transmission Tx-Tx OR reflection Rx-Rx are in principle indistinguishable, and exhibit quantum interference by a null in coincidence counts, since the photons always go to same detector.

Note that the high spectral entanglement in frequency yields no distinguishing information to path events.

Figure 8. Hong-Ou-Mandel interferometer single SPDC source.

the wave packets of the two photons are coherent with one another, they will always exit the same port of the BS because their probability amplitudes cancel and lead to destructive interference.

In Fig. 9 we show the HOMI effect setup in a dual-bus MRR, which now has an extra (upper) external bus from which another photon can enter and exit. This was also discussed and analyzed in [Alsing-Hach17a]. The two entry ports are labeled as a, b (lower and upper), while the two exit ports are labeled as c, d (lower and upper). Note that an input photon on port a can exit after several full- or half-round trips on port c or d , respectively. The analysis in Fig. 9 shows the operator input fields a, b written of the operator output fields c, d so that one can transform an input quantum state (written in terms of operators a, b acting on the vacuum) into an output state (written in terms of operators c, d acting on the vacuum). Note that the HOMI effect is the *permanent* of matrix $\text{Perm}(M)$, of this input to output transformation, which is a general feature of the a generalized n -photon interference effect. We will discuss the results of this HOMI effect in MRR in Section 4.6.

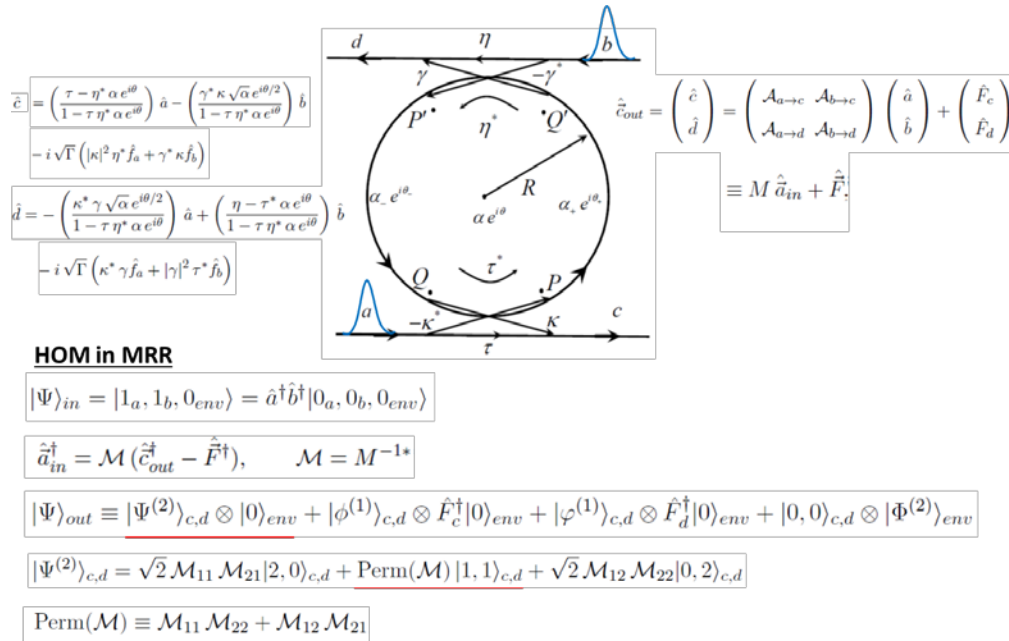
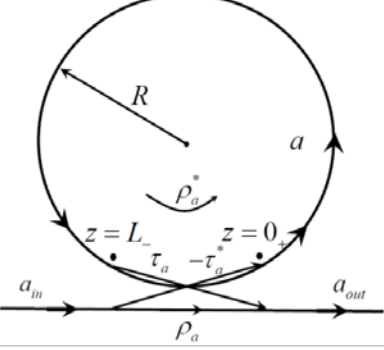


Figure 9. Hong-Ou-Mandel Interference effect in MRR.

Entangled Photon Generation inside a MRR.

In a pair of papers [Alsing-Hach17b,c] Alsing and Hach (see also the discussion in [Schneeloch18]) considered the biphoton generation processes of SPDC and SFWM (spontaneous four wave mixing) inside a MRR, as shown in Fig 10. Again, the internal signal and idler fields inside the MRR can be eliminated to yield the output field $\vec{a}_{out}(\omega) = (a_{signal}, b_{idler})$ in terms of the input fields (taken to be in the vacuum state) and the quantum noise fields: $\vec{a}_{out}(\omega) = G(\omega)\vec{a}_{in}(\omega) + H(\omega)\vec{f}_a(\omega)$. From Fig. 5 one can see the effects of the cavity round trips through the Fabry-Perot-like terms $S_{k=(a,b)}$ in the transfer matrices $G(\omega)$ and $H(\omega)$. Note that while standard Langevin approaches assume specific forms for the commutators of the noise operators, Alsing and Hach



$$\mathcal{H}^{NL} = \int_{-\infty}^{\infty} \frac{d\omega}{2\pi} g(\omega) (\alpha_p(z, \omega) a^\dagger(z, \omega) b^\dagger(z, \omega) + \alpha_p^*(z, \omega) a(z, \omega) b(z, \omega))$$

$$g(\omega) = g_{spdc}(\omega) = \frac{3(\hbar\omega_c)^{3/2}\chi^{(2)}}{4\epsilon_0\tilde{n}^4V_{ring}}, \quad \text{for SPDC,}$$

$$g(\omega) = g_{sfwm}(\omega) = \frac{3(\hbar\omega_c)^2\chi^{(3)}}{4\epsilon_0\tilde{n}^4V_{ring}}, \quad \text{for SFWM,}$$

$$(-i\omega + v_a\partial_z) a(z, \omega) = -ig\alpha_p(z, \omega) b^\dagger(z, \omega) - \frac{\gamma'_a}{2} a(z, \omega) + \alpha_{polz} f_a(z, \omega),$$

$$(-i\omega + v_b\partial_z) b^\dagger(z, \omega) = ig\alpha_p^*(z, \omega) a(z, \omega) - \frac{\gamma'_b}{2} b^\dagger(z, \omega) + \alpha_{polz} f_b(z, \omega).$$

$$\vec{a}_{in}(\omega) = \begin{pmatrix} a_{in}(\omega) \\ b_{in}^\dagger(\omega) \end{pmatrix}, \quad \vec{a}_{out}(\omega) = \begin{pmatrix} a_{out}(\omega) \\ b_{out}^\dagger(\omega) \end{pmatrix}, \quad \vec{f}(\omega) = \begin{pmatrix} f_a(\omega) \\ f_b^\dagger(\omega) \end{pmatrix}$$

$$\vec{a}_{out}(\omega) = G(\omega) \vec{a}_{in}(\omega) + H(\omega) \vec{f}(\omega)$$

$G(\omega)$: Classical Phenomenological Loss α (Yariv, Rabus)	$H(\omega)$: Quantum Noise Loss
$G(\omega) = \begin{pmatrix} G_{aa}(\omega) & G_{ab}(\omega) \\ G_{ba}(\omega) & G_{bb}(\omega) \end{pmatrix},$ $\equiv \frac{1}{D} \begin{pmatrix} (e^{i\xi_a L} - \rho_a)(1 - \rho_b e^{i\xi_b L}) + r_a r_b \rho_a & -i r_a \tau_a \tau_b e^{i\xi_b L} \\ i r_b \tau_b \tau_a e^{i\xi_a L} & (e^{i\xi_b L} - \rho_b)(1 - \rho_a e^{i\xi_a L}) + r_a r_b \rho_b \end{pmatrix}$	$H(\omega) = \begin{pmatrix} H_{aa}(\omega) & H_{ab}(\omega) \\ H_{ba}(\omega) & H_{bb}(\omega) \end{pmatrix} = \frac{1}{D} \begin{pmatrix} \tau_a(1 - \rho_b e^{i\xi_b L}) & -i r_a \tau_a \\ i r_b \tau_b & \tau_b(1 - \rho_a e^{i\xi_a L}) \end{pmatrix}$

$$D = (1 - \rho_a e^{i\xi_a L})(1 - \rho_b e^{i\xi_b L}) - r_a r_b, \quad r_a = g\alpha_p T_a, \quad r_b = g\alpha_p^* T_b,$$

$$\alpha_k = e^{-\gamma'_k/2 T_k}, \quad \theta_k = \omega T_k, \quad \text{for } k \in \{a, b\}, \quad e^{i\xi_k L} \equiv \alpha_k e^{i\theta_k}$$

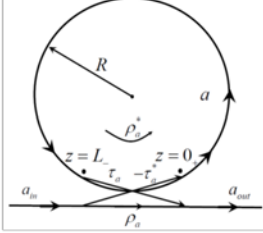
$$S_k = \frac{1}{1 - \rho_k e^{i\xi_k L}} =$$

$$\sum_{n=0}^{\infty} (\rho_k e^{i\xi_k L})^n \equiv \sum_{n=0}^{\infty} (\rho_k \alpha_k e^{i\theta_k})^n$$

Figure 10. Entangled biphoton generation (SPDC and SFWM) inside a MRR.

did not have to. Fig. 11 shows that to ensure overall unitarity the requirement that the commutators of the output of the signal and idler fields (a_{out}, b_{out}) obey the canonical form (given that the input fields (a_{in}, b_{in}) do) is enough to determine completely the commutation relations of the internal quantum noise operators $\vec{f}_a = (f_a, f_b)$. As Fig. 11 shows, these noise commutators do not need to commute in general (as is often assumed), but do commute if the roundtrip time of the signal and idler are assumed to be identical.

$$\begin{aligned} [a_{out}(\omega), a_{out}^\dagger(\omega')] &= \delta(\omega - \omega') \Rightarrow |H_{aa}|^2 C_{aa} - |H_{ab}|^2 C_{bb} + 2\text{Re}(H_{aa} H_{ab}^* D_{ab}) = 1 - (|G_{aa}|^2 - |G_{ab}|^2), \\ [b_{out}(\omega), b_{out}^\dagger(\omega')] &= \delta(\omega - \omega') \Rightarrow -|H_{ba}|^2 C_{aa} + |H_{bb}|^2 C_{bb} + 2\text{Re}(H_{ba} H_{bb}^* D_{ab}) = 1 - (|G_{bb}|^2 - |G_{ba}|^2), \\ [a_{out}(\omega), b_{out}(\omega')] &= 0 \Rightarrow H_{aa} H_{ba}^* C_{aa} - H_{ab} H_{bb}^* C_{bb} + H_{aa} H_{bb}^* D_{ab} + H_{ab} H_{ba}^* D_{ab} = G_{ab} G_{bb}^* - G_{aa} G_{ba}^*, \\ [a_{out}(\omega), b_{out}^\dagger(\omega')] &= 0 \Rightarrow \det(H) C_{ab} = 0, \end{aligned}$$



four constants $C_{aa}, C_{bb}, C_{ab}, D_{ab}$

$$\begin{aligned} [f_a(\omega), f_a^\dagger(\omega')] &= C_{aa} \delta(\omega - \omega'), & [f_b(\omega), f_b^\dagger(\omega')] &= C_{bb} \delta(\omega - \omega'), \\ [f_a(\omega), f_b^\dagger(\omega')] &= C_{ab} \delta(\omega - \omega'), & [f_a(\omega), f_b(\omega')] &= D_{ab} \delta(\omega - \omega'). \end{aligned}$$

$$C_{kk}(\omega) = 1 - \alpha_k^2 - |r_k|^2 = 1 - e^{-\gamma'_k T_k} - |g\alpha_p T_k|^2 \xrightarrow{\text{high Q}} \gamma'_k T_k - |g\alpha_p T_k|^2, \quad k \in \{a, b\},$$

$$D_{ab} = i(r_b^* - r_a) = ig\alpha_p(T_b - T_a),$$

Figure 11. Commutators for quantum noise operators inside a MRR.

Ultimately, what is important for experimental investigation is the biphoton output state $\psi_{ab}^{(2)}(\omega)$ comprising the signal and idler photons within the MRR, when one traces out the effect of the internal quantum noise $\vec{f}_a = (f_a, f_b)$. This is shown in Fig. 12, where ρ_{ab} is the reduced density

Biphoton state inside the mrr

$$\psi_{ab}^{(2)}(\omega) = e^{i\theta_p(\omega)} G_{aa}^*(\omega) G_{bb}(\omega) + e^{-i\theta_p(\omega)} G_{ab}(\omega) G_{ba}^*(\omega)$$

$$\approx e^{i\theta_p(\omega)} G_{aa}^*(\omega) G_{bb}(\omega) \quad (e^{-i\theta_p(\omega)} G_{ab}(\omega) G_{ba}^*(\omega) \propto |g \alpha_p T_{ab}|^2)$$

Reduced Density Matrix $\rho_{ab} = \text{Tr}_{env}[\Psi]_{out} \langle \Psi |]$

$$\rho_{ab} = \int_{-\infty}^{\infty} \frac{d\omega}{2\pi} |\Psi^{(2)}(\omega)\rangle_{ab} \langle \Psi^{(2)}(\omega)| + |r_{ab}(\omega)|^2 \left(\int_{-\infty}^{\infty} \frac{d\omega}{2\pi} R_0(\omega) |0\rangle_{ab} \langle 0|, \right.$$

$$\left. + \int_{-\infty}^{\infty} \frac{d\omega}{2\pi} |\phi_a^{(1)}(\omega)|^2 C_{bb}(\omega) |1_\omega, 0\rangle_{ab} \langle 1_\omega, 0| + \int_{-\infty}^{\infty} \frac{d\omega}{2\pi} C_{aa}(\omega) |\phi_b^{(1)}(\omega)|^2 |0, 1_\omega\rangle_{ab} \langle 0, 1_\omega| \right)$$

$$|\Psi^{(2)}(\omega)\rangle_{ab} = [2\pi \delta(\omega) - i|r_{ab}(\omega)| C_{vac}(\omega)] |0\rangle_{ab} - i|r_{ab}(\omega)| \psi_{ab}^{(2)}(\omega) |1_\omega, 1_{-\omega}\rangle_{ab},$$

$$R_0(\omega) = C_{aa}(\omega) C_{bb}(\omega) |e^{i\theta_p(\omega)} H_{aa}^*(\omega) H_{bb}(\omega) + e^{-i\theta_p(\omega)} H_{ab}(\omega) H_{ba}^*(\omega)|^2.$$

$$\text{Tr}_{env} [f_a^p(\omega') \langle \text{vac} |_{env} \langle \text{vac} | f_i(\omega) = \langle \text{vac} |_{env} \langle \text{vac} | f_i(\omega) f_a^p(\omega') \langle \text{vac} |_{env} = [C_{i,p} \delta(\omega - \omega'),]$$

$$[f_i, f_i^\dagger] = [f_i, f_i^\dagger] + f_i^\dagger f_i$$

$$[\langle \text{vac} |_{env} \langle \text{vac} | f_i(\omega) f_j(\omega) f_i^\dagger(\omega') f_j^\dagger(\omega') \langle \text{vac} |_{env} = [C_{i,i}(\omega) C_{j,j}(\omega) + C_{i,j}(\omega) C_{j,i}(\omega)] \delta(\omega - \omega')]$$

Figure 12. Reduced density matrix for the biphoton output state within a MRR.

matrix for the signal-idler subsystem. Terms other than $\psi_{ab}^{(2)}(\omega)$ in ρ_{ab} indicate the effects of the loss of one or both photons. Rates for coincidence to accidentals, heralding efficiency and biphoton generation rates are shown and discussed in Section 4.6.

3.7 Analysis of Quantum Algorithms for the DWAVE: background and theory

Quantum Annealing (QA) is based on classical simulated annealing, in which the system tends towards the ground state while the temperature is lowered. Also QA adds the non-classical process of quantum tunneling to avoid being trapped in local minima. QA is not generally expected to promise exponential speedup over conventional (classical) algorithms, however it does offer the potential for speedup over conventional algorithms for computational hard combinatorial optimization problems with spikey "energy landscapes". The D-Wave system uses the fundamentals of quantum annealing and superconducting qubits to tackle solving complex computing problems across many domains, including but not limited to training deep neural networks, sampling for machine learning, pattern recognition and combinatorial optimization.

Our research focused on an in-depth exploration of a variety of graph theory NP-Complete combinatorial optimization problems solved over the class of de Bruijn graphs. The NP-complete problems we explored include the maximum cut problem, vertex cover problem, graph partitioning problem, maximum clique problem, independent set problem graph coloring problem, clique cover, Hamilton cycle problem, Steiner tree, directed feedback vertex set, feedback edge set, and undirected feedback vertex set. One can envision an optimization problem represented as a graph, with the nodes or vertices representing the variables, and the edges the interactions (couplings) between the variables. Graphs that are fully connected (an edge between every pair of nodes)

represent hard optimization problems both conventionally and for quantum annealers; the latter because it is hard to physically fabricate interactions between every qubit. Thus our choice of this class of graphs is based on the sparsity of these graphs. Our aim was in determining which graph problems are embedded and solved most efficiently on the D-Wave architecture. For each problem we formally defined the task, determined the bounds of the optimal solution, developed the Quadratic Unconstrained Binary Optimization (QUBO) formulation, embedded the problem on a 128-qubit D-Wave chip, ran the problem on D-Wave's 2000Q chip and provided brute force solutions for comparison.

An example of the steps taken to solve the vertex cover problem on the de Bruijn graph $B(2,3)$ are demonstrated below (see Fig. 13). First, the vertex cover problem is stated as given an

Graph	Size	De Bruijn Graph	n=2	n=3	n=5	n=7
$B(2,2)$	2	d=2	Nodes: 4 Cover: 2	Nodes: 8 Cover: 5	Nodes: 32 Cover: 19	Nodes: 128 Cover: 73
$B(3,2)$	6	d=3	Nodes: 9 Cover: 6	Nodes: 27 Cover: 18	Nodes: 243 Cover: 146	Nodes: 2187 Cover: 1250
$B(d,2), d \geq 4, d \text{ even}$	$d^2 - \frac{d^2}{4}$	d=4	Nodes: 16 Cover: 12	Nodes: 64 Cover: 43	Nodes: 1024 Cover: 615	Nodes: 16384 Cover: 9363
$B(d,2), d \geq 5, d \text{ odd}$	$d^2 - \frac{d^2 - 1}{4}$	d=5	Nodes: 25 Cover: 19	Nodes: 125 Cover: 84	Nodes: 3125 Cover: 1876	Nodes: 78125 Cover: 44644
$B(d,3)$	$d^3 - \frac{d^3 - d}{3} - 1$	d=6	Nodes: 36 Cover: 27	Nodes: 216 Cover: 145	Nodes: 7776 Cover: 4667	Nodes: 279936 Cover: 159965
$B(d,5)$	$d^5 - \frac{2(d^5 - d)}{5} - 1$					
$B(d,7)$	$d^7 - \frac{3(d^7 - d)}{7} - 1$					

Figure 13. The exact values for the size of a minimum vertex cover in (d, n) .

undirected graph $G = (V, E)$, find the smallest subset $V' \subseteq V$ such that for every edge $uv \in E$ at least one of u and v belongs to V' [Garey79]. Then we determined through literature searches the Next we can begin to formulate the vertex cover problem into the QUBO form needed to embed the problem onto the D-Wave hardware. theoretical optimal solution bounds of the vertex cover

QUBO Formulation

- Variable $x_i = 1$ if and only if vertex $i \in S$
- Smallest set we can find: $\min \sum x_i$ for $i \in V$
- Every edge is covered: $\min \sum (1 - x_u)(1 - x_v)$ for $uv \in E$

$$\min \sum_{i \in V} x_i + \sum_{uv \in E} (x_u x_v - x_u - x_v)$$

Figure 14. The QUBO formula for the vertex cover problem.

problem, shown in Fig. 1, in order to verify that the answer given by the D-Wave machine is reasonable.

As can be seen in Fig. 14 the first term looks for the smallest set possible while the second term ensures that every edge has at least one endpoint in the set. Once in this form we must embed and run the program. We used the built in embedding function for the D-Wave, *sapiEmbedding()*, on the *c4-sw_sample* solver which provides 128 qubits. Figure 15 provides pseudocode to generate the vertex cover QUBO coefficients.

Algorithm 2 Vertex Cover QUBO Coefficients Generator

```

1: procedure VCQ(AdjMat)
2:    $N \leftarrow$  number of nodes
3:    $Q \leftarrow \text{zeros}(N, N)$ 
4:   for  $i = 1 : N$  do
5:      $Q(i, i) \leftarrow Q(i, i) + A$ 
6:     for  $j = i + 1 : N$  do
7:       if  $ij \in E$  then
8:          $Q(i, j) \leftarrow Q(i, j) + B$ 
9:          $Q(i, i) \leftarrow Q(i, i) - B$ 
10:         $Q(j, j) \leftarrow Q(j, j) - B$ 
11:   return  $Q$ 

```

Figure 15. Pseudocode to generate Vertex Cover QUBO coefficients.

4.0 RESULTS AND DISCUSSION

4.1 Aluminum Nitride (AlN) quantum circuits: fabrication and experiments

The first significant step to move forward with the wide bandgap photonics platform is to describe the AlN on sapphire photonics fabrication process. The process begins with an unpatterned AlN-on-sapphire chip diced up from a whole wafer. Next is to spin coat HSQ (2% XR-1541), pattern using electron beam lithography, and develop using an aqueous mixture of 1 wt % NaOH and 4 wt % NaCl for high contrast. The followings steps are: (i) etch by ICP-RIE using chlorine chemistry, (ii) strip HSQ, (iii) clad with silicon oxynitride using plasma-enhanced chemical vapor deposition (PECVD), (iv) Edge polish for making the inverse-tapered edge couplers. After completion of the fabrication process the device are checked with a scanning electron microscope (SEM) as shown in the image of a fabricated AlN waveguide (c). The measured device correlates well with the required dimensions given by the waveguide simulations. The simulated transversal component of TE mode in AlN waveguide for PMMA and SiON cladding for 638 nm (top) and 400 nm (bottom) wavelengths is shown in Fig. 16. The devices in Fig. 16 demonstrate the various essential optical components, designed for top-cladding with either (i) Poly(methyl methacrylate) (PMMA), which has a refractive index of $n \sim 1.5$ in UV to visible wavelengths, or (ii) silicon oxynitride (SiON), with a refractive index matched to the underlying sapphire $n = 1.76$ by adjusting the composition of

oxygen and nitrogen to achieve a refractive index between that of silica (1.45) and silicon nitride (2.1).

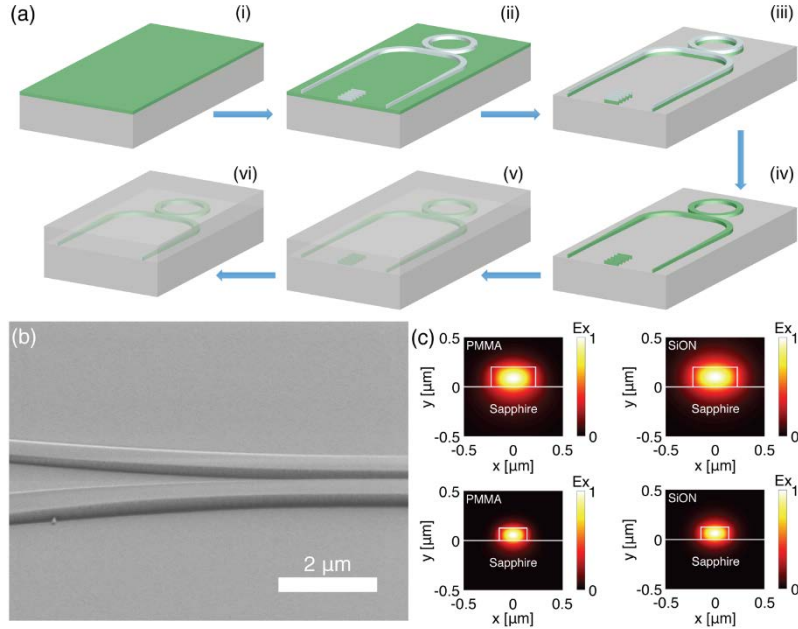


Figure 16. Fabrication of the AlN material platform.

Specific details of the fabrication process are described here. The process starts off with an unpatterned 1 cm x 1 cm AlN-on-sapphire chip diced from a whole wafer. Next, 5 nm thick Cr discharge layer is deposited via electron beam evaporation. Then, after oxygen plasma treatment under 100 W for 3 minutes to improve electron beam resist adhesion, hydrogen silsesquioxane (2% XR-1541) is spun on. The hydrogen silsesquioxane (HSQ) film thickness is measured to be 70 nm by using an AFM to measure the step feature profile after patterning. The patterns are written with an Elionix ELS-F125 electron beam lithography system at 125 keV using a dose of 10,000 C/cm². The patterns are developed using a salty developer, which is an aqueous mixture of 1 wt % NaOH and 4 wt % NaCl, for high contrast [Yang07].

After HSQ mask patterning, the pattern is first transferred to the Cr layer at an etch rate of 55 nm/min by electron cyclotron resonance reactive-ion etching (ECR-RIE) using a gas mixture of Cl₂/O₂ (3:1 ratio) at 300 W ECR power, 30 W RF Bias power, 10 mTorr pressure, and 25C. Then, the AlN waveguides and photonic components are etched by inductively coupled plasma reactive-ion etching (ICP-RIE) using a gas mixture of BCl₃/Cl₂/Ar in two steps. The first step is for etching the native aluminum oxide at an etch rate of 5 nm/min using BCl₃/Ar (2:1 ratio) at 120 W ICP power, 40 W RF Bias power, 7.5 mTorr pressure, and 40C. The second step is for etching the AlN at an etch rate of 200 nm/min using Cl₂/Ar (4:1 ratio) at 360 W ICP power, 100 W RF Bias power, 5 mTorr pressure, and 40C. We do not observe a significant change in the surface roughness from

the etching, and a sidewall angle close to 90 degrees is achieved due to the combination of physical sputtering and plasma chemical etching. The Cr and HSQ are lastly removed with Cr etchant and buffered oxide etch (BOE), respectively. Figure 2 (b) shows a scanning electron microscope (SEM) image of the fabricated AlN waveguide. Finally, the waveguides are clad with approximately 3 microns of SiON using plasma-enhanced chemical vapor deposition (PECVD) by the parameters shown in Table 1 or spin coated with approximately 2 microns of PMMA. In the case where the chip is cladded with SiON, the edges of the chip are mechanically polished back to the inverse-tapered waveguides for edge coupling.

Table 1. Fabrication parameters for the AlN material platform.

LF Power (W)	Pulse Time (s)	HF Power (W)	Pulse Time (s)	Chamber Pressure (mTorr)	Chamber Temperature (°C)	SiH ₄ (sccm)	NH ₃ (sccm)	N ₂ O (sccm)	N ₂ (sccm)
160	12	200	8	1900	350	20	70	50	1425

The two methods used to couple light into and from the QPIC are shown in figure 3: grating couplers and inverse-tapered edge couplers. Due to the narrow frequency response of grating couplers, two different grating couplers are used for testing components in the visible wavelength from 500 nm to 700 nm wavelength: a green wavelength grating coupler optimized for 500 nm to 600 nm (shown in the top SEM image of Fig. 3 (a)) and a red wavelength grating coupler optimized for 600 nm to 700 nm (shown in the bottom SEM image of Fig. 17 (a)). Fig. 17 (b), (c) show comparisons between the simulated and experimentally measured transmission spectra for the green and red wavelength grating couplers, respectively. The general shape of the experimental grating coupler wavelength response matches well with simulation. The experimental coupling efficiencies are listed in arbitrary units because we do not experimentally mode-match the spatial modes of the grating coupler and collection objective.

Both green and red wavelength grating couplers are optimized for TE polarization, so the simulated coupling efficiencies model the collection of TE polarized light injected into the 450 nm wide by 200 nm tall AlN waveguide on bulk sapphire and scattered by the grating coupler. For the green wavelength grating coupler, the first gap width is 60 nm and the first grating period is 285 nm. Then, the gap width and grating period both linearly increase from 101 nm and 325 nm to 150 nm and 346 nm, respectively (increasing linearly in each period for 17 periods). Finally, the gratings maintain a gap width of 150 nm and grating period of 346 nm for the remaining 9 periods. In a similar fashion, for the red wavelength grating coupler, the first gap width is 60 nm and the first grating period is 285 nm. Then, the gap width and grating period both linearly increase from 101 nm and 401 nm to 132 nm and 414 nm, respectively (increasing in each period for 10 periods).

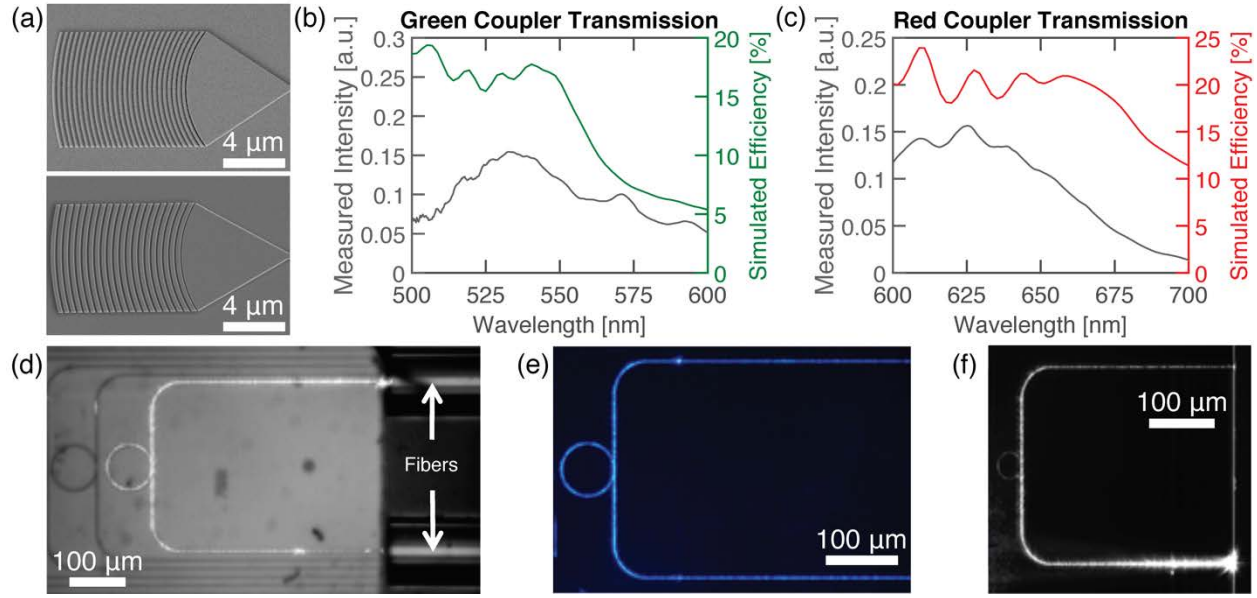


Figure 17. Coupling methods for the AlN waveguides.

Finally, the gratings maintain a gap width of 132 nm and grating period of 414 nm for the remaining 10 periods. For both the green and red wavelength grating couplers, the dimensions of each individual grating periods are optimized in order for the spatial mode profile of the diffracted light to be a Gaussian field profile. The grating couplers are also designed to be cladded with PMMA, rather than simple air cladding, in order to increase the out-of-plane coupling efficiency by pulling more of the optical mode away from the underlying sapphire substrate as PMMA has a higher

refractive index than air. Both grating couplers are designed for an etch depth of 200 nm in order for ease of fabrication so that the grating couplers and waveguides can be fabricated in the same steps with no additional processing. Therefore, we believe grating couplers with even higher collection efficiency can be achieved with partially etched gratings. As well as the grating couplers, fiber edge coupling to the waveguides at 369.5 – 468 nm using was completed using Nufern SM300 fiber. The third coupling method was free-space edge coupling using aspheric lenses at 468 and 369.5 nm, respectively. The inverse-tapered waveguides adiabatically transform and expand the AlN waveguide mode to the fiber waveguide mode at the chip's edge facet.

Looking back at Fig. 17 (c), it shows the simulated electric field profiles of the AlN waveguide modes for PMMA and SiON cladding for 400 nm and 638 nm wavelengths. The waveguides support a single transverse electric (TE) mode for their respective wavelengths. Wrapping these waveguides into rings produces the high Q resonators. The ring resonator measurements are summarized in Fig. 18. Also, in Fig. 18 (b) shows the response at 369.5 nm of the 40 μm radius ring resonator around resonance; a Lorentzian fit indicates a Q of >24,000. Since the resonance is very under-coupled, the ring resonance cannot be measured directly through an access bus waveguide in this case. Rather, the resonance is measured from light scattering from the ring and

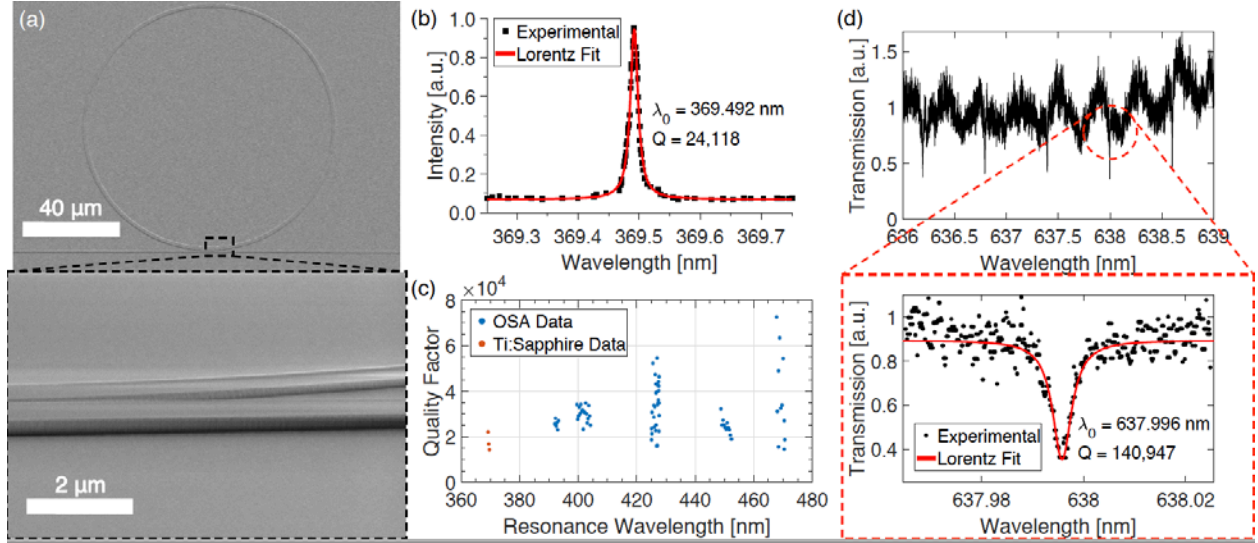


Figure 18. Resonances from the AlN micro-ring resonators.

into an objective above the resonator and detected using an UV sensitive camera. Hence, the data show a resonance peak rather than a dip. The plot in Fig. 18 (c) shows the quality factors of 40 μm radius ring resonators measured using an optical spectrum analyzer (OSA) for wavelengths spanning from 380 nm to 480 nm, along with the quality factors at 369.5 nm using both a frequency doubled pulsed Ti:Sapphire laser (Spectra-Physics Mai Tai) and a continuous-wave (CW) tunable Ti:Sapphire laser (M Squared SolisTiS). If we assume that the propagation loss is dominated by the sidewall scattering loss and linear absorption loss of the material, then we can estimate the propagation loss using the following equation for calculating the loss rate α given the resonator Q , where $n(g)$ is the group index [Miller17, Yariv02, Yariv00, Levy11, Dutt17]:

$$Q = \frac{2\pi n_g}{\lambda \alpha} \quad (5)$$

Then, the loss can be calculated by:

$$\text{loss} = 10 \log_{10}(e^{-\alpha}) \quad (6)$$

To calculate the loss in units of dB/cm, λ in Eq. 5 should be in units of cm. Thus, the Q of $>24,000$ at 369.5 nm wavelength corresponds to a propagation loss of 75 dB/cm, where we measure the $n(g)$ to be 2.45 experimentally from the Free-Spectral-Range (FSR) of the ring. The frequency response of a 50 μm radius ring resonator around resonance in the red wavelength range is shown as well in Fig. 18. We probe the 50 μm radius ring with an evanescently coupled access waveguide. The Lorentzian fitting shows a loaded Q of $>140,000$ at 638 nm. In order to obtain the intrinsic Q of the ring resonator, we can use the following [Miller17, Yariv00, Yariv02, Levy11, Dutt17]:

$$Q_i = \frac{2Q_l}{1 \pm \sqrt{T_0}} \quad (7)$$

Where Q_i is the intrinsic Q, Q_l is the loaded Q, T_0 is the normalized transmitted power at the resonance wavelength, and the + and - signs correspond to under- and over-coupled regimes, respectively. Since the ring resonator is operating in the undercoupled regime, we find the intrinsic Q to be >170,000, which corresponds to a propagation loss of 4.9 dB/cm. These ring resonators are useful for measuring the waveguide propagation loss (in the undercoupled regime). In the critically coupled regime, or in a drop-port configuration, they serve as on-chip filters as needed for filtering atomic fluorescence, for example [Mouradian15]. They can also be used for on-chip photon pair generation [Guo17].

Distributed Bragg reflectors (DBRs) represent another important QPIC component as broadband on-chip reflectors and filters. To further support this point, we develop a distributed Bragg reflector with high extinction for 532 nm for use as on-chip filtering of the excitation pump light used for exciting NV centers in diamond. The DBR has a period of 140 nm with 50 % duty cycle, and it is designed to have an adiabatic tapering from the regular waveguide into the DBR in order to have low insertion loss. Also, the DBR is designed to structurally have rounded features for ease of fabrication. Figure 19(a) shows an SEM image of the fabricated DBR. The overlay blue plot in Fig. 19 (b) shows the simulated transmission spectrum for the DBR, which has 45 dB extinction for the 532 nm green pump light. The black plot in Fig. 19(b) shows at least 15 dB extinction experimentally for the DBR. We expect the extinction to be even higher because the attenuated 532 nm signal was at the noise floor of our experimental system.

Figure 19(c) shows a directional coupler with a 50/50 splitting ratio, which is the integrated photonics equivalent of a free space beamsplitter. Directional couplers coherently couple between adjacent waveguide modes and can be used as a building block for Mach-Zehnder interferometers (MZIs) [Mower15]. Figure 5(d) shows the power at the output two arms of the directional coupler as the coupling length is swept. A coupling length of 14 um results in a 50/50 splitting ratio.

Theoretically, for a pair of coupled waveguides with the same geometry and dimensions, the fraction of cross-coupled power K is given by the following, where Δn is the effective refractive index difference between the symmetric and antisymmetric supermodes and L is the length of the directional coupler [Mikkelsen14]:

$$K = \sin^2(\pi L \Delta n / \lambda) \quad (8)$$

By using a mode solver to calculate Δn and solving for Eq. 3 to get 50/50 splitting ratio ($K = 0.5$), we get that L should be 23 um. However, this does not take into account the coupling from one waveguide into the other as the two waveguides are brought to the desired separation of 200 nm in the evanescent coupling region via waveguide bends. In simulating the full directional coupler structure with the evanescent waveguide coupling region and bent region, we find a

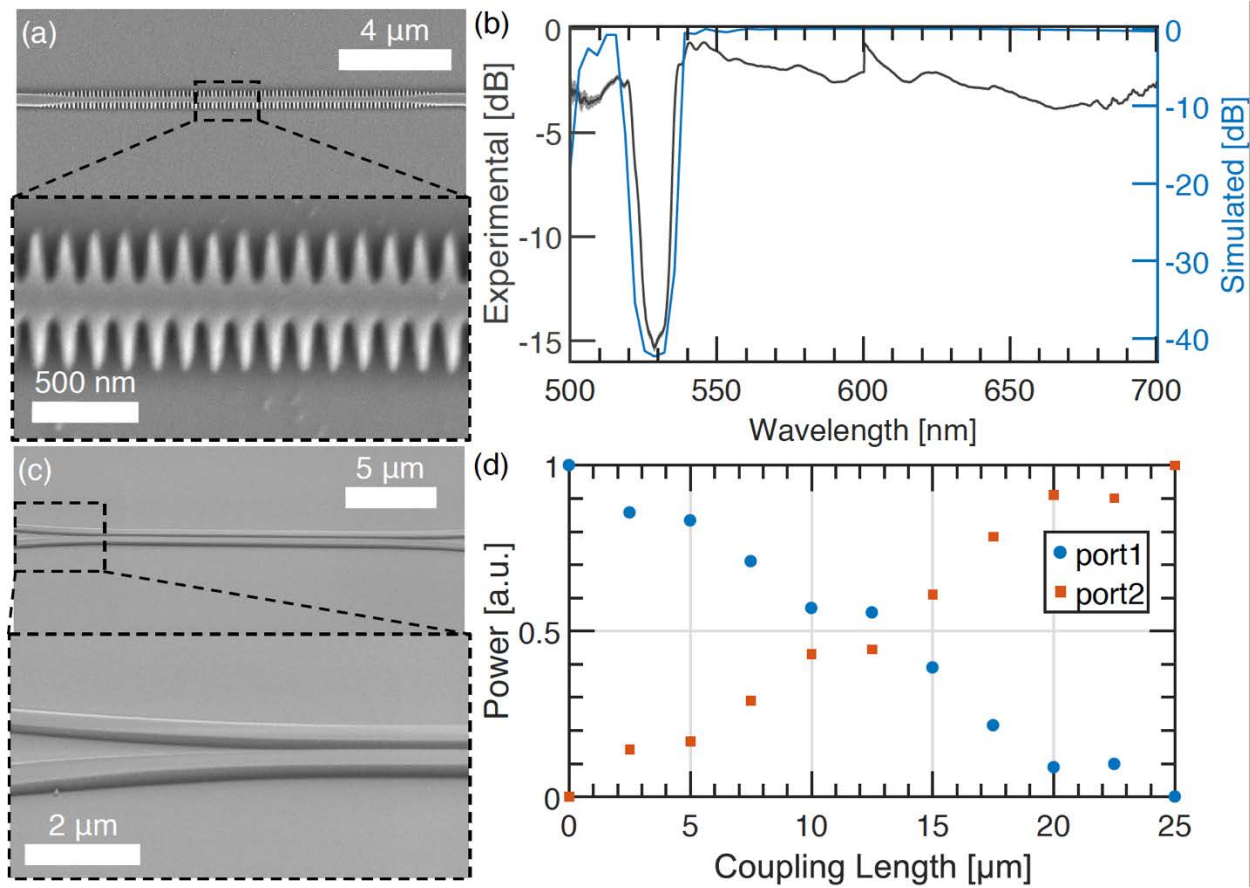


Figure 19. DBR and directional coupler in AlN.

coupling length of 14 μm necessary for achieving 50/50 splitting, matching well to the experimental result.

The UV propagation loss shown here at 369.5 nm is several tens of orders of magnitude lower than the propagation loss shown by Stegmaier et al. for 400 nm wavelength in an AlN on SiO₂ platform [Stegmaier14]. Furthermore, the crystalline materials in our AlN on sapphire platform allow for refined Raman and other parasitic processes to be localized and minimized [Liu17]. Although the UV single mode propagation loss presented here is higher than that shown in SiN-on-SiO₂ multimode and planar waveguides for wavelength at the lower end of the visible spectrum [Gorin08, Hoffman16] and silica-on-silicon waveguides in theory for UV and VIS [Oh17, Lee11], SiN-on-SiO₂ and silica-on-silicon platforms are limited to passive components and thermo-optic tuners [Heck14]. Furthermore, silica waveguides are typically a couple of microns in dimension with large bend radii and are not ideal for compact, high-density, large-scale photonic integration. Hence, our AlN on sapphire platform, to date, has the record-low waveguide propagation loss down to UV wavelength for active optical materials with $\chi^{(2)}$ properties and supports chip-scale, compact, CMOS-compatible integration [Stegmaier14, Poberaj09]. Nonetheless, we believe that there are many sources of loss that can be eliminated or improved upon. One of the main causes

for the propagation loss is interface scattering from the roughness of the AlN waveguide sidewalls from etching. To reduce the propagation loss by a few orders of magnitude, one can engineer the waveguide dimensions such that the optical mode overlaps minimally with the sidewalls so that the light scatters minimally from the waveguide's faces [Miller17]. Furthermore, the current waveguide fabrication is optimized for vertical sidewalls so that the photonic components experimentally match well with the simulated design. As such, the reactive-ion etching necessitates a fast physical etch that causes the sidewalls to be rougher than could be possible with a more chemical etch. Sidewall roughness of less than 0.1 nm is often the benchmark for achieving interface scattering close to that of the bulk scattering limit of optical materials [Schroeder73]. It may be possible to further optimize the etching parameters to reduce loss. In addition, there is an inherent roughness of the top surface of the AlN thin film from the unoptimized growth. As AlN grown on top of sapphire is still not at the level of silicon on insulator (SOI) wafers made by Smart-Cut technology used in conventional integrated photonic platforms [Aspar01], we expect there to

be room for improvements. Finally, the AlN thin film we use is crystalline in the growth direction and polycrystalline in the in-plane direction. Replacing this material with a completely crystalline AlN thin film grown on top of sapphire should result in a lower dislocation density and defect density, thereby improving the purity of our material so that it would behave closer to what is expected of bulk AlN. Furthermore, the crystallinity of single-crystal AlN grown on top of sapphire has been shown to improve significantly by high temperature annealing [Miyake16]. All of these properties combined provides a versatile platform for photonics from the ultraviolet to the infrared.

4.2 A Quantum Photonic Processor (QPP): experiments

Experiments in integrated optics at telecom wavelengths under this project focused on two thrust. The largest effort was placed on the development of the Quantum Photonics Processor or QPP [Mower15]. The second was an experiment based on the famous Hong-Ou-Mandel dip.

The QPP was developed and fabricated in a close collaboration with the Massachusetts Institute of Technology [Mower15,Harris15]. It consists of 88 fully independently controlled 2x2 Mach-Zender Interferometers (MZI). They are configured as nearest neighbors between 26 input and 26 output modes. This creates a massive reconfigurable circuit that can be used to implement a diverse set of operations with potential application to Air Force relevant problems. These include quantum computing tasks, dense coding and communication protocols, and quantum walk based search operations.

The efforts under this project are two fold first to calibrate and test the device itself in the in-house quantum optics lab and second to effectively package the chip into a usable form factor that can be taken outside the lab.

The QPP is fabricated though a CMOS compatible processes using Silicon on insulator (SOI) chips. This means that the device is thermally tunable by applying a voltage to a resistive heater integrated into the device. However the MZI's are extremely sensitive to fabrication

inconsistencies such as the resistance of the heating element, and the roughness of the waveguide sidewalls. Therefore each MZI has a different response to a given applied voltage and each MZI must be individually calibrated to give the correct response. As the MZI cannot be tested individually a method was needed to calibrate a single MZI in a large array of MZI's. In conjunction with MIT an initial version of software was developed to calibrate and operate the QPP. Upon testing at AFRL's in house quantum lab multiple deficiencies were found in the existing software, including inefficient device drivers, slow operations and inaccuracy calibration. We undertook it to write a completely new suite of software for the calibration and operation of the device.

During the effort to create a new calibration software we discovered two significant design flaws in our device the first is that many of the ground leads for the MZI's were tied directly together on the chip itself to reduce the number of ground pins (and wire bonds) required. [Prabhu18] This has the negative consequence of created ground loops in our circuits. Thus applying a voltage to a particular MZI creates a smaller voltage on all of the MZI's which share the same ground lead. This creates a small but measureable inaccuracy in the calibration of the total system and it is extremely difficult to account for in software alone.

The second design flaw is that the optical input and output of the device are on opposite sides of the chip. This is opposed to routing the input and output of the device to the same edge facet. This may seem like a minor inconvenience but having two couplers double the work required to optically align the system. It decreases the stability of the system and increases the risk the chip and fibers might collide and cause damage.

These issues lead to a new design for a second generation QPP which avoids these issues. The new device has unique input and ground pins for each and every MZI. The input and output are on the same edge of the chip. This design was made in collaboration with Rochester Institute of tech. (RIT) and the group of Stephan Preble. New chips were fabricated and several have been delivered to AFRL for initial testing.

The second area of effort is the packaging of this and other optical chips. These devices while very small and light weight on their own still have a SWAP problem. Namely the equipment required to operate them in the current "laboratory state" is bulky and impractical. The chips are electrically tuned and therefore require being wire bonded to a PCB. The devices require a few micron's worth of alignment precision of the optical input fibers to the chip's waveguide. The chips are also fragile and sensitive to debris similar to CMOS computer chips. With these constraints what we need for a practical and fieldable device is a hermetically sealed package containing the wire bonded chip and PCB as well as permanently aligned and fixed fiber to waveguide coupler.

The current laboratory setup consists of the wire bonded chip, two 6 axis optical alignment stages and a microscope. The total size and weight of the setup is approximately 1 square meter and 20

lbs. While this is fine for testing in a lab it needs to be miniaturized for a practical and fieldable device.

As a part of this project we contracted and coordinated with three companies to create a packaging solution for the current version of the QPP. This included a source of custom PCBs designed to cope with the large number of required wire bonds (over 200) in such a small area. We went through several iterations of designs of a test mount for the chip and PCBs in conjunction with the wire bonding company and the optical alignment company. This has resulted in one device being wire bonded and mounted. It is currently with the finally company for the alignment and affixing of the input and output fibers. This operation will hopefully be completed by the end of the year and the packaged device can be tested at the AFRL in house lab.

4.3 Quantum Frequency Conversion: experiments

There are several compelling factors that show that the ability to change the frequency (or color) of a single photon will be an essential technology for quantum computing. One reason for this lays in the nature of quantum bits or Qbits. Many Qbits have excellent characteristics for storing information but are not feasible to transfer information long distances at non trivial speed. Photons are the only qubit with the ability to carry information at high speed.

A second issue is that qubits such as trapped ions themselves adsorb different wavelength than they emit. Thus a photon emitted by a single ion cannot be easily adsorbed by a second ion [Kurz16]. This is a result of the fundamental structure of the elections in each species of atom or ion and is unavoidable.

A third consideration is that no two different types of qubits operate at the same wavelengths. Thus any realistic hybrid qubit environment will require efficient frequency conversion as and translation or interface stage between the different qubits.

We are performing an experiment on quantum frequency conversion at the single photon level based on the ions trap experiments underway at AFRL. The ion trap experiments are based on Ytterbium ions witch emitted in the ultraviolet range at 370nm. This wavelength is not suitable for many applications. This is due to the high energy photons being easily adsorbed. Previous work in this area was only somewhat successful, with an academic group producing 0.2% efficient frequency conversion at the single photon level. While this is a low level of efficiency, the loss due to adsorption of UV is extremely high per kilometer of fiber. Thus we only need a few percent of quantum frequency conversion efficiency to have a higher photon rate than using UV.

The in house experiments are based on Difference Frequency Generation (DFG) in Lithium Niobate LN [Bock18,Rutz16]. The conversion process requires conservation of energy and momentum. DFG is a 3rd order process in which a single photon in mixed with a high intensity pump wavelength. This creates a pump photon and a third photon with a wavelength that is equal to the difference between the source and the pump, satisfying conservation of energy. To satisfy

the momentum conservation we need a special material called Periodically Poled Lithium Niobate PPLN. Periodic poling refers to the alignment of a dipole in the crystal structure which is alternately aligned in the +Z or -Z direction. This poling aligns the dipole such that the momentum of the interaction is conserved. It also allows for long crystals (3-4cm) which increase the interaction length and there for the efficiency of the conversion. The main difficulty in this version of DFG is that the polling period must be very narrow to satisfy the conservation of momentum constraint. In particular it must be 2.34um per period. This is a difficult size to produce and is significantly smaller than what is used in industry.

We worked with two commercial manufactures and one academic group to source high quality crystals with the required polling period. We have established an experimental test setup in the in house quantum optics lab. We are working on the alignment and test of the conversion are planned before the end of the calendar year.

4.4 A Dual Mach Zehnder Interferometer: fabrication and experiments

The dual Mach-Zehnder interferometer (MZI) coupled ring introduced in section 3.4 has been fabricated and it has undergone preliminary experimental verification. The device) was fabricated at the AIM photonics foundry and an example is presented in the Fig. 20 below. The device has two input ports given by the top left (bottom right.) These inputs lead to a counter-clockwise propagating resonance within the ring device and dropped signal at the top right (bottom left.)

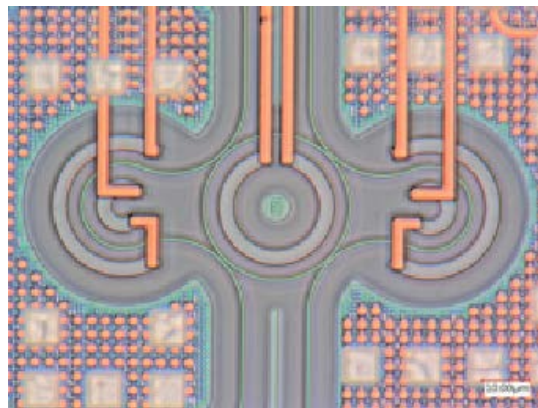


Figure 20. Fabricated dual MZI ring resonator.

To combat fabrication errors, we included active length adjustments to the device by P-doping silicon over one micron away; a process which makes the silicon conductive. Applying a typical voltage of 7V leads to approximately 70mW of dissipated power near the silicon waveguide. This localized heating increases the index of the silicon waveguide via the thermo-optic effect and gives us a full free-spectral range tuning to the device. The spacing of one micron between heater element and optical waveguide leads to negligible coupling from the waveguide.

The propagation loss of the waveguide is close to 3.5dB/cm which is typical for this process. We designed the waveguide to be single mode at the central wavelength of 1550nm and the radius was chosen such that the free-spectral range of the ring is on the order of 5nm. After thermally tuning the device we measured the resonance spectra as shown in the Fig. 21 below where the input-through (add-drop) plot are measured by measuring power transmitted across the device as a function of wavelength from the top left (right) to the bottom left (right) waveguides of the device. The resonances manifest themselves as dips in the transmitted power while the blue, green, and red bands indicated the desired blue shifted, pump and red shifted wavelength signals, respectively. Therefore, with an input pump in the green band, we expect to collect light in wavelengths of the red and blue bands.

We designed this device to not only separate the pump photons from the generated signal photons, but also to eject the signal photons with a higher efficiency than typically possible in a ring resonator device. We can visually verify the success of our device operation by noting the pump photons are almost entirely lost inside the ring (>90% power visibility between the wavelengths that are on and off resonance.) Therefore, the pump photons are almost critically coupled and experience the highest level of resonant enhancement within the ring. Conversely, the blue and red bands only see a 50% visibility between maximal transmission and minimal transmission. As mentioned in section 3.4, the lower visibility leads to a lower resonant enhancement but equates to a lower intrinsic loss for the photons that are generated in the ring. Our choice of 50% visibility is a compromise between enhancing the photon generation process and the quality of the collected signals.

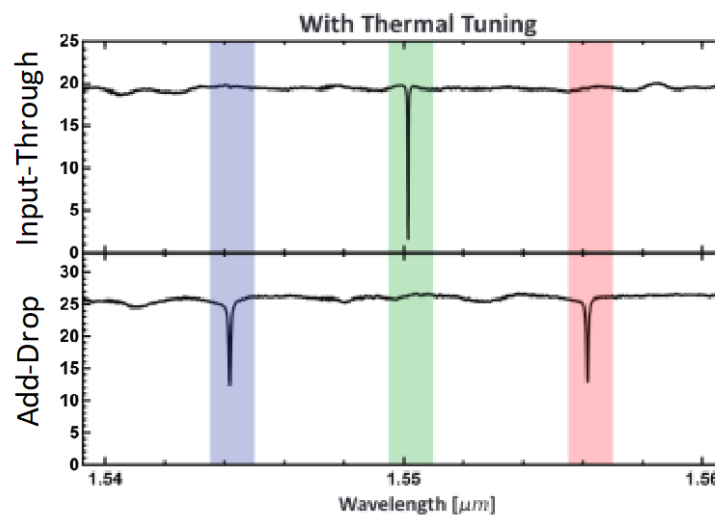


Figure 21. Resonance spectra of fabricated resonator.

We have verified the behavior of the MZI ring resonator follows this high-level explanation by measuring what we have come to call the coincidence ratio. The coincidence ratio is a dimensionless number which relates the total detected coincidences from photons generated by the device to the port combinations of coincidences generated by the device. Since we are pumping

with a single pump wavelength, the signal has two wavelengths associated with it. We use off-chip filters to separate the red and blue bands of the generated photons for both the through and drop ports. The two colors and two port choices give a total of 4 combinations which can be taken into consideration.

In Fig. 22 below, we present our measured results of these coincidences. The pump is injected on the through port side of the device and as a function of time between detection events on the two signal bands, we form histograms. The total measured coincidences of photons detected where both photons came out the drop port is over two orders of magnitude higher than all other even permutations. In fact, we find a coincidence ratio of over 97%. In other words, 97% of detected photon pairs generated by the device couple out the drop side as a pair. We contrast this to a double bus device with symmetric coupling which would only see 25% of detected photon pairs making their way out of the drop side.

These results are published in [Tison17] and make a step towards efficient, pump filtered, pure sources on a SOI platform. Changing the way that we pump the device, (i.e. pumping on the add side of the ring) leads to photons which do not share spectral correlations as predicted in [Vernon17]. The verification of such a result is in the plans for future experiments entailing this ring source. Once verified, the device can be considered for experiments based on the “heralding” of single photons. There needs to be no spectral correlations in the photon pairs generated otherwise the detection of one photon would lead to a mixed state on the other, destroying the assumption of pure states later in the experiment.

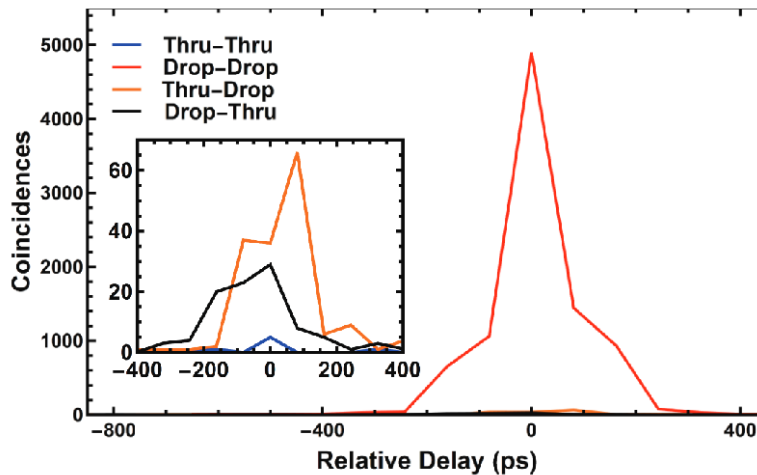


Figure 22. Coincidence ratio of MZI ring

4.5 Analysis of Spontaneous Parametric Down Conversion (SPDC): experiments

As described in Section 3.5, we authored a comprehensive tutorial and analysis of Spontaneous Parametric Down-Conversion, where among other results, we derived formulas for the absolute pair-generation rate in experiments utilizing degenerate, collinear SPDC. More important than,

this, we also tested the validity of these formulas with three different experiments. The first experiment tested the generation rate for type-0 SPDC in a periodically-poled bulk medium, of biphotons coupled into a single-mode optical fiber. The second experiment tested the generation rate for type-I SPDC in a bulk crystal, collected over all spatial modes. The third experiment tested the generation rate for type-II SPDC in a periodically poled single-mode nonlinear waveguide also coupled into single-mode optical fiber.

The first challenge over all of these experiments is to successfully back out the raw pair generation rate R from the experimentally recorded signals rate R_1 , the idlers rate R_2 , their respective background noise rates Φ_1 , Φ_2 , the coincidence count rate R_{12} and its corresponding background accidentals rate A_{12} as illustrated in Fig. 23 below.

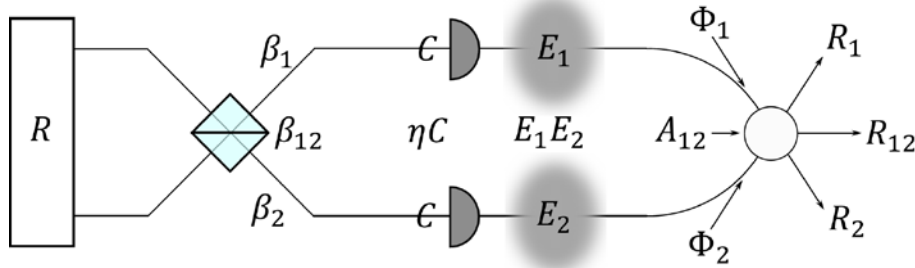


Figure 23. Diagram of efficiencies, losses, and generation rates in a generic SPDC experiment.

To accomplish this, it was important to be aware that not all sources of loss were uncorrelated between signals and idlers. For example, the heralding efficiency η is the conditional probability that the idler photon will couple into the single-mode fiber conditioned on the signal photon coupling successfully. This efficiency is distinct from the coupling efficiency C , describing the fraction of light incident on the single-mode fiber that couples inside. On top of this, we introduces uncorrelated efficiencies E_1 , and E_2 describing losses in the signal and idler channels which that their joint effect on reducing coincidences is $E_1 E_2$. On top of this, a non-polarizing beamsplitter will have a correlated effect on reducing signals, idler, and coincidences, by fractions β_1 , β_2 , and β_{12} , respectively. With this parametrization, the signals, idlers, and experimental coincidence rates are related to the raw rate as follows:

$$R_1 = R \cdot E_1 \cdot C \cdot \beta_1 + \Phi_1 \quad (9)$$

$$R_2 = R \cdot E_2 \cdot C \cdot \beta_2 + \Phi_2 \quad (10)$$

$$R_{12} = R \cdot E_1 \cdot E_2 \cdot \eta \cdot C \cdot \beta_{12} + A_{12} \quad (11)$$

From these relations, one can obtain the raw rate R , through some algebra to get:

$$R = \frac{(R_1 - \Phi_1)(R_2 - \Phi_2)}{(R_{12} - A_{12})} \left(\frac{\beta_{12}}{\beta_1 \beta_2} \right) \frac{\eta}{C} \quad (12)$$

From this relation, the task of finding the raw rate R is relatively straightforward, as the beamsplitter losses ($\beta_1, \beta_2, \beta_{12}$) can be directly measured experimentally, and we do not need to characterize the uncorrelated losses E_1, E_2 at all. However, obtaining the heralding efficiency η and coupling efficiency C is a more challenging endeavor due to the low power of the generated down-converted light. For example, 100 million photon pairs per second at 1550nm is among the brightest flux one can obtain for one milliwatt of CW laser power, but this biphoton flux only amounts to approximately 26 picowatts, which is barely above what classical optical power meters (as opposed to photon counters) are capable of registering. With the experimental optics known, the heralding efficiency η can be evaluated from theory [Bennink10, Dixon14] given the focal spot

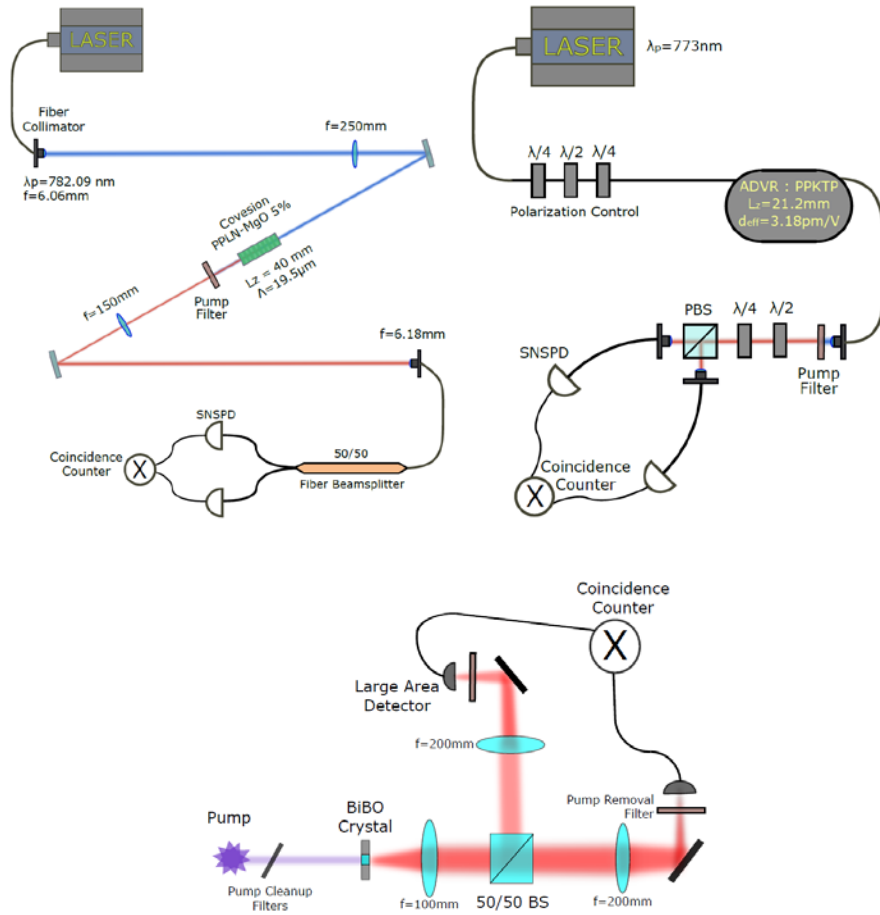


Figure 24. Diagrams of type-0, type-II (single-mode), and type-I (free space) biphoton sources.

size and Rayleigh range of the pump light in the nonlinear medium, and these corresponding parameters for the down-converted light, back-propagated from the accepting mode-field diameter of the exiting optical fiber. Similarly, the coupling efficiency C can be estimated with measurements of a parallel experiment where bright light at the down-converted wavelength is used in conjunction with optics to emulate the beam parameters in the original experiment. It was these methods that we used for our experiments.

For our first experiment (top left in Fig. 24), we coupled a 782.09nm OBIS laser into a single-mode fiber, which was collimated with a triplet Fiber Collimator and focused with a 250mm AR-coated lens. The fiber collimator functioned together with the focusing lens to approximately reproduce a telescope imaging system where the pump beam came to a focus at the center of a PPLN nonlinear crystal with standard deviation $52.6\mu\text{m}$, a wide enough spot size that the beam is considered collimated over the 40mm length of the crystal. The crystal was stationed in a temperature-controlled oven to fine-tune the phase matching of the crystal, and to keep its temperature more stable. The down-converted light exiting the crystal passes through a similar telescope-imaging system to optimize the amount of light coupling into the exit single-mode fiber. From there, the light is split with a 50/50 fiber beamsplitter, and directed to Superconducting-Nanowire Single-Photon-Detectors (SNSPDs), where the photon pair statistics are recorded through coincidence counting measurements. Because this experiment is accurately modeled by our theoretical treatment of type-0 collinear degenerate SPDC in a single Gaussian spatial mode with a Gaussian pump beam and a periodically poled crystal, we were able to achieve remarkable correspondence between theory and experiment. Where our theoretical prediction was a brightness of $(94.86 \pm 10.89) \times 10^6$ pairs per second per mW of pump power, the experimental result was $(95.63 \pm 2.71) \times 10^6/\text{s}/\text{mW}$, a disagreement of less than one percent. The relatively large uncertainties is due to the propagation of error of over a dozen variables in the formulas for the theoretical prediction.

For our second experiment (bottom center in Fig. 24), we illuminated a 1.0mm-long Bismuth Borate (BiBO) nonlinear crystal with 405nm light from an OBIS laser to generate 810nm down-converted light through type-I SPDC. We used a bulk 50/50 beamsplitter, and both collimating and focusing optics to direct as much of the down-converted light onto large area single-photon detectors, whose statistics were recorded with coincidence counting. In this experiment, extracting the raw rate R was much more straightforward as the coupling and heralding efficiencies are 100 percent when all of the down-converted light is being collected (detector efficiencies notwithstanding). The greater challenge is in developing a theoretical formula that accurately models this experiment since it requires accurately calculating the inner product between the full biphoton wavefunction and the zero-order Gaussian wavefunction so as to obtain the total rate R through the single-mode rate and the relative probability that the biphoton will be in the zero-order Gaussian mode. While the accuracy of our theoretical model is contingent on the accuracy of our estimation of the biphoton wavefunction, we were able to justify a valid approximation (See [Schneeloch18] for details), and get relatively decent agreement between the theoretical rate of $(53.87 \pm 10.87) \times 10^6/\text{s}/\text{mW}$ and the experimentally measured rate of $(64.68 \pm 1.69) \times 10^6/\text{s}/\text{mW}$.

For our third experiment (top right in Fig. 24), we coupled a Newport NewFocus external cavity diode laser at 773nm into a single-mode nonlinear waveguide made through the diffusion of a dopant into a Periodically Poled Potassium Titanyl Phosphate (PPKTP) crystal to create a graded index profile. This waveguide was used to produce photon pairs at 1546nm through type-II SPDC.

The light exiting the laser in a single-mode fiber passes through fiber polarization rotators to ensure that the light entering the waveguide is vertically polarized. The waveguide itself is bonded to the single-mode fibers at both ends. The light exiting the exit fiber is collimated and passes through polarization rotators before being split with a polarizing beam splitter (PBS). Because the photon pairs created in type-II SPDC are mutually orthogonal, they can be split with near-unity efficiency with a PBS. After this, the light is coupled into SNSPDs and their statistics is recorded by coincidence counting. With the manufacturer's quoted specification for the coupling efficiency C and the mode field diameter of the down-converted light, and the optical properties of PPKTP, we estimated a theoretical pair generation rate of $(23.58 \pm 5.60) \times 10^6/s/mW$, while the experimental pair generation rate was $(35.5 \pm 0.08) \times 10^6/s/mW$, a significant difference. Upon further questioning, it became clear that the diffusion of dopant in the nonlinear waveguide is asymmetric, yielding oblong pear-shaped eigenmodes instead of the circularly symmetric Gaussian modes of the waveguide. While augmenting the theory to describe elliptical Gaussian modes produced a more accurate prediction, this experiment along with the two previous ones clearly show how the extent to which the model the theory relies on well-describes the experiment is critical in obtaining good agreement between theory and experiment

4.6 Nonlinear optical processes in micro-ring resonators (MRR): results

Hong-Ou-Mandel Manifolds

As discussed in Section 3.6 and in Fig. 9, Alsing and Hach analysis a generalization of the Hong-Ou-Mandel Interference (HOMI) effect in mirroring resonators (MRR), in the presence of quantum noise (internal scattering losses). In the standard bulk-optic version of the HOMI effect using beam splitters (BS), there is a single point solution for maximal destructive interference which occurs for 50/50 BS (i.e. transmission coefficient amplitude $\tau=1/\sqrt{2}$). In the case of the MRR, essentially the form single BS has been replaced by two BS, a lower and an upper one, of transmission coefficient amplitudes τ, η respectively. In addition there another new parameter θ , the internal round trip phase accumulation, where $\theta = m2\pi$ indicates the MRR is on resonance i.e. maximum internal field amplitude, while $\theta = (2m + 1)\pi/2$ indicates the operation in the middle of MRR FSR (free spectral range), i.e. minimal internal field amplitude. In effect, the parameter space (τ) of the bulk optic BS has been replaced by the expanded parameter space of (τ, η, θ) . Therefore, the MRR version of the HOMI effect allows for a 2D manifold of solutions, as shown in Fig. 25, for various amounts of loss. As examined in Fig. 25, the HOMI manifold of solution persists even under the presence of 5%-10% losses (typically, loss in MRR are on the order of 1% at best).

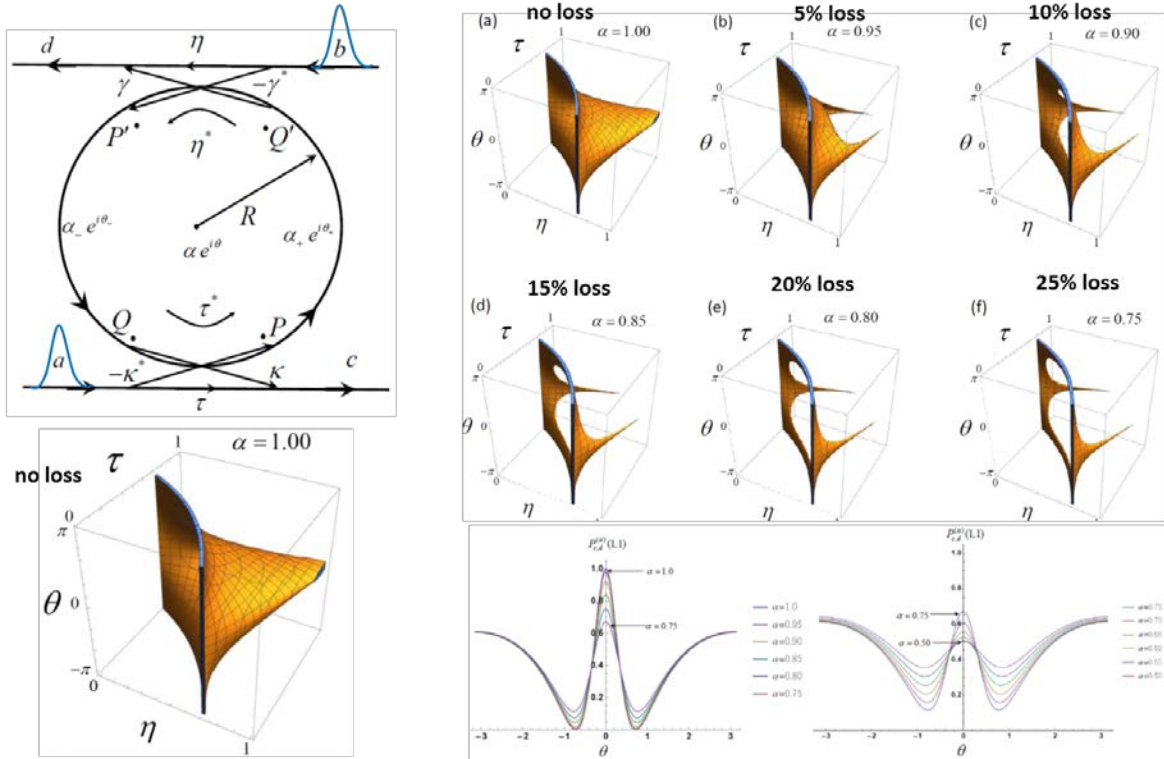


Figure 25. Hong-Ou-Mandel Interference manifolds in MRR including internal loss.

Figure 26 shows an in-house designed and AIM (American Institute of Manufacturing) fabricated

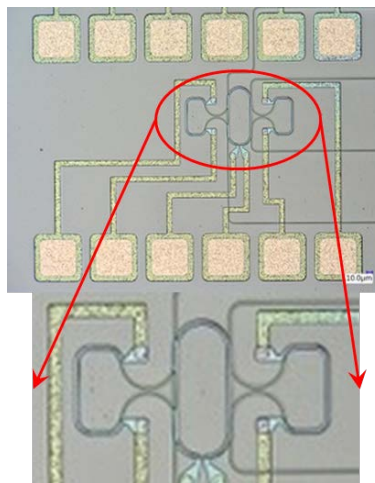


Figure 26. In-house designed and AIM fabricated MRR to test HOMI-manifolds prediction. MRR to test the HOMI-manifold prediction. The MRR in Fig. 26 appears as a vertical racetrack oval (see enlargement), while the two side ring loops are additional MZI (Mach Zehnder Interferometers) used to adjust the phase of the left and right arms (i.e. 90 degree rotate version of lower and upper MRR legs in Fig. 9). The 12 brown squares are electrical contacts for voltages

used to adjust the MZIs and set (τ, η, θ) . Experimental setup has begun in-house as of the writing of this report and results will be reported elsewhere in scientific literature.

Entangled Photon Generation inside a MRR.

Figure 27 shows the coincidence-to-accidental (CAR) rate (top) and single photon heralding efficiency (bottom) for SPDC inside a MRR, as discussed in Section 3.6. These rates depend on

$$1\text{mW } (\chi^{(2)} \sim 2 \times 10^{-12} \text{ m/V}, \alpha_p \sim 10^3 \text{ V/m}), R = 20\mu\text{m}, T_k \sim 1 \text{ ps} \\ r_p \sim 10^{-5}$$

Coincidence to Accidental (CAR) Rate

$$R_{\text{CAR}}^{(\text{out})}(\omega) = \frac{|\psi_{ab}^{(2)}(\omega)|^2}{|\phi_a^{(1)}(\omega)|^2 C_{bb}(\omega) + C_{aa}(\omega) |\phi_b^{(1)}(\omega)|^2} \\ \xrightarrow{\text{high Q } \mathcal{O}(|g| \alpha_p)} \frac{|G_{aa}^*(\omega) G_{bb}(\omega)|^2}{|G_{aa}^*(\omega) \tilde{H}_{bb}(\omega)|^2 + |\tilde{H}_{aa}^*(\omega) G_{bb}(\omega)|^2} \\ = \left(\frac{\gamma_a \gamma'_a}{\omega^2 + (\Delta_a/2)^2} + \frac{\gamma_b \gamma'_b}{\omega^2 + (\Delta_b/2)^2} \right)^{-1}$$

Heralding Efficiency Rate

$$R_{\text{herald}}^{(\text{out})}(\omega) = \frac{|\psi_{ab}^{(2)}(\omega)|^2}{|\phi_a^{(1)}(\omega)|^2 C_{bb}(\omega) + |\psi_{ab}^{(2)}(\omega)|^2} \\ \xrightarrow{\text{high Q } \mathcal{O}(|g| \alpha_p)} \frac{|G_{aa}^*(\omega) G_{bb}(\omega)|^2}{|G_{aa}^*(\omega) \tilde{H}_{bb}(\omega)|^2 + |G_{aa}^*(\omega) G_{bb}(\omega)|^2} \\ = \left(1 + \frac{\gamma_b \gamma'_b}{\omega^2 + (\Delta_b/2)^2} \right)^{-1}$$

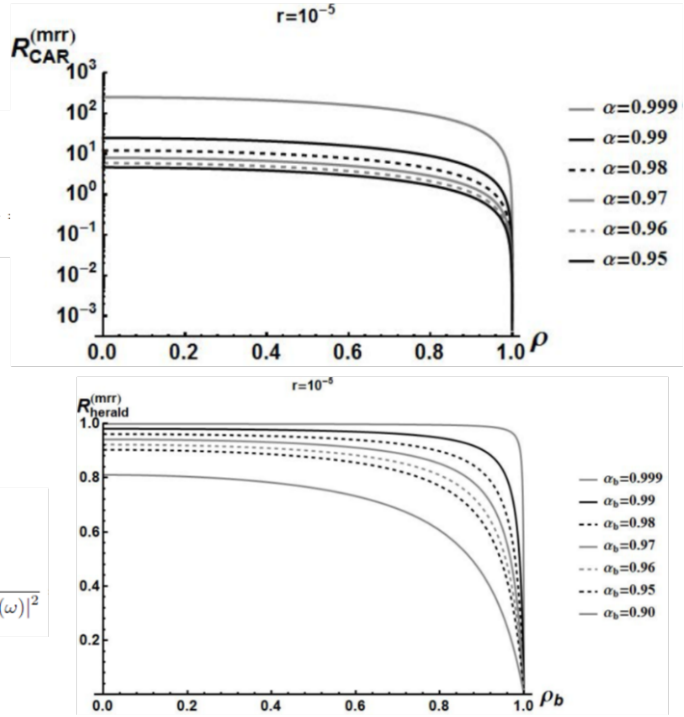


Figure 27. CAR and heralding efficiency rates inside the MRR.

three factors: (i) the biphoton wavefunction amplitude $\psi_{ab}^{(2)}(\omega)$, and (ii) the singles rates for the signal photon $\phi_a^{(1)}(\omega)$ with the noise rate $C_{bb}(\omega)$ for a lost (scattered) idler, and similarly (iii) the singles rates for the idler photon $\phi_b^{(1)}(\omega)$ with the noise rate $C_{aa}(\omega)$ for a lost (scattered) signal photon, photons. The CAR is the ratio of the probability (i.e. squared quantum amplitude) for the presence of a biphoton $|\psi_{ab}^{(2)}(\omega)|^2$, to the totals singles rate (both signal and idler) $|\phi_a^{(1)}(\omega)|^2 C_{bb}(\omega) + |\phi_b^{(1)}(\omega)|^2 C_{aa}(\omega)$. The single photon heralding efficiency (say to herald the signal photon by detecting the idler photon) is again the ratio of the biphoton rate $|\psi_{ab}^{(2)}(\omega)|^2$ but now to $|\phi_a^{(1)}(\omega)|^2 C_{bb}(\omega) + |\psi_{ab}^{(2)}(\omega)|^2$ which represents the sum of the photon rates for detecting the single signal photon, but also with detected biphotons. In Fig. 28 we show the

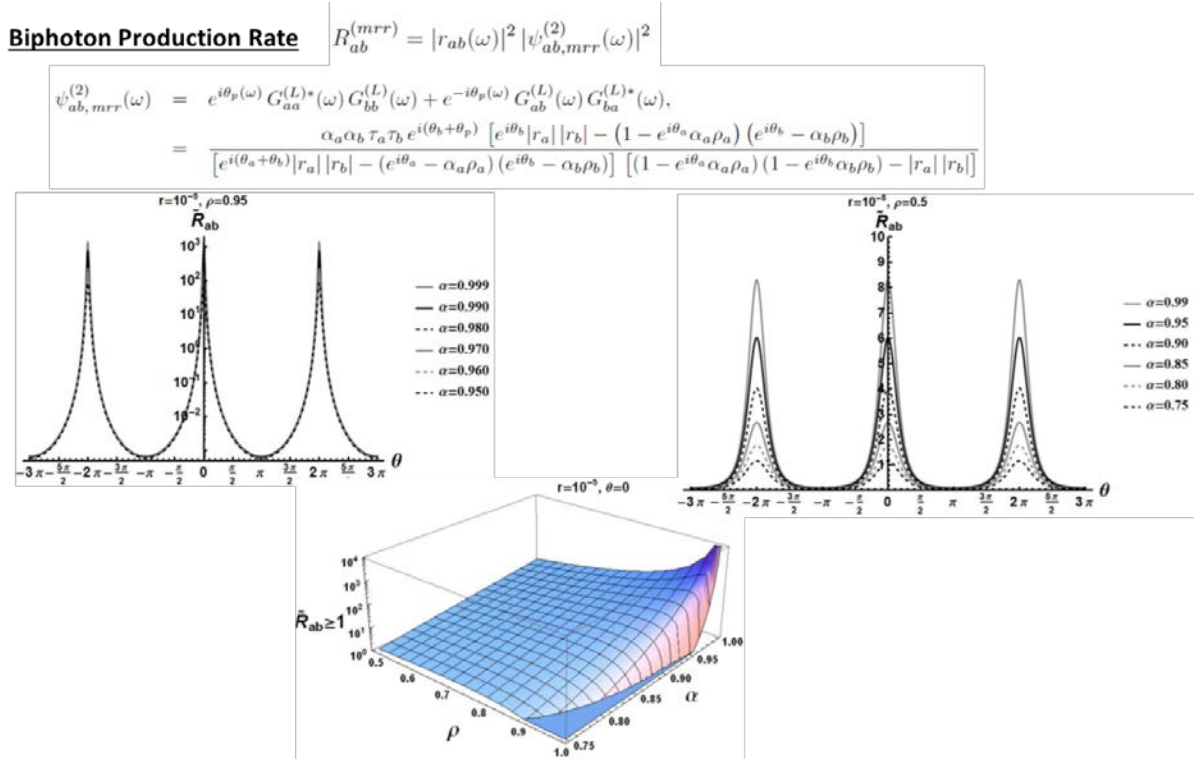


Figure 28. Biphoton production rate inside the MRR.

biphoton production rate $|\psi_{ab}^{(2)}(\omega)|^2$ itself for various values of the reflection coefficient ρ and nonlinear coupling coefficient (for SPDC, appearing in the Hamiltonian) r . The effect of the Fabry-Perot-like resonances of the MRR is clearly evident. The strong MRR resonances when θ is an integer multiple of π ultimately justifies the use the standard Langevin approach to cavity input-output analysis, though the formulation by Alsing and Hach is valid for fields off (and very far off) resonance (agreeing with the former on and near resonances).

4.7 Analysis of Quantum Algorithms for the DWAVE: assessment

First we want to recall that the embeddings are run using a heuristic algorithm and therefore result in variations in the number of qubits required, as each run a different embedding is given. In de Bruijn graphs, $B(d, n)$, the parameter d indicates how connected the graph is. Thus when using the 128-qubit solver the *sapiEmbedding()* function has more trouble embedding graphs with $d > 2$. For de Bruijn networks, we were able to find embeddings for the vertex cover problem with the characteristics shown in Fig. 29.

Graph	Nodes	QUBO Variables	Qubits	Max Chain Length
$B(2, 3)$	8	8	12	2
$B(3, 2)$	9	9	23	3
$B(2, 4)$	16	16	35	3
$B(4, 2)$	16	16	54	5
$B(5, 2)$	25	25	—	—
$B(3, 3)$	27	27	93	5
$B(2, 5)$	32	32	88	5
$B(6, 2)$	36	36	—	—
$B(2, 6)$	64	64	—	—
$B(4, 3)$	64	64	—	—
$B(3, 4)$	81	81	—	—

Figure 29. Embedding characteristics of vertex cover being solved on de Bruijn graphs.

We show an embedding for $B(2,5)$ in Fig. 30, where we can notice that $B(2,5)$ is a graph with 32 nodes, 32 QUBO variables and 88 qubits are used to embed the graph into the chimera structure.

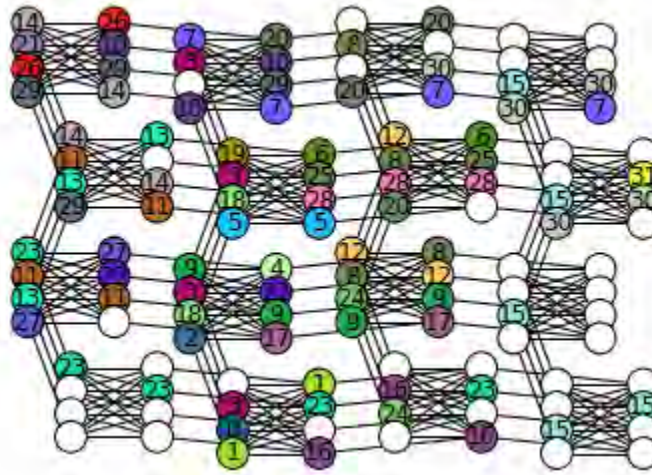


Figure 30. Embedding of the Vertex Cover QUBO for graph $B(2,5)$.

Next in Figure 31 we provide a comparison of the D-Wave result found and the optimal solution from literature for some of the larger instances that fit and we were able to run on the D-Wave architecture.

Problem	Graph	Found	Literature	Optimal
Maximum Cut	$\mathcal{B}(8, 2)$	336	≥ 272	
	$\mathcal{B}(4, 3)$	192	≥ 144	
	$\mathcal{B}(3, 4)$	192	≥ 142	
	$\mathcal{B}(2, 7)$	226	≥ 160	
Vertex Cover	$\mathcal{B}(8, 2)$	48	48	
	$\mathcal{B}(5, 3)$	100	84	
	$\mathcal{B}(3, 4)$	57	≤ 57	
	$\mathcal{B}(2, 7)$	85	73	
Graph Partitioning	$\mathcal{B}(8, 2)$	162	≥ 128	
	$\mathcal{B}(4, 3)$	64	≥ 35	
	$\mathcal{B}(2, 6)$	18	≥ 7	
Maximum Clique	$\mathcal{B}(8, 2)$	3	3	3
	$\mathcal{B}(4, 3)$	3	3	3
	$\mathcal{B}(2, 6)$	3	3	3
Independent Set	$\mathcal{B}(8, 2)$	16	16	
	$\mathcal{B}(4, 3)$	21	21	
	$\mathcal{B}(2, 6)$	27	≥ 25	
Graph Coloring	$\mathcal{B}(3, 2)$	5	≤ 4	4
	$\mathcal{B}(2, 4)$	4	≤ 4	3
Clique Cover	$\mathcal{B}(3, 2)$	3	≤ 4	3
	$\mathcal{B}(2, 3)$	3	≤ 5	3
Hamilton Cycle	$\mathcal{B}(2, 3)$	Yes	Yes	Yes
	$\mathcal{B}(2, 3)$	Yes	Yes	Yes
Steiner Tree	$\mathcal{B}(2, 2), U = \{1, 2\}$	2		2
	$\mathcal{B}(2, 2), U = \{1, 4\}$	3		3
Dir FB V Set	$\mathcal{B}(2, 3)$	3	≤ 5	3
FB E Set	$\mathcal{B}(2, 2)$	2	≤ 6	2
Undir FB V Set	$\mathcal{B}(2, 2)$	1	1	1

Figure 31. Comparison of D-Wave results found to literature optimal solutions.

We can see that due to the chimera structure of the D-Wave systems architecture sparse graphs are needed. As the graphs grow chains of qubits are needed to recreate the connectivity needed and relatively quickly the graphs cannot be embedded into the machine. Moving forward we are continuing to monitor as the D-Wave produces larger scale systems with the potential for better connectivity to see what problems (specifically Air Force relevant problems) can fit on the system. We are also beginning to research the new NISQ gate-based quantum processors, simulators and software. Our analysis will include how we program a gate-based quantum processor, do NISQ gate-based quantum processors provide a quantum advantage, what problems are they good at solving and what Air Force relevant problems could be solved on these processors.

5.0 CONCLUSIONS

A summary of the AlN results compared to research in the literature is shown in Table 2 specifically geared towards research that is chip-scale and highly compact, particularly AlN on SiO₂ and SiN on SiO₂. This work shows the highest demonstrated resonator Q factor in the UV, as well as higher VIS resonator Q factor than in previous AlN on SiO₂ work [Xiong12]. As the AlN thin film shown in this work is crystalline with fewer absorptive defects and dislocation density than the polycrystalline AlN in previous work, AlN on sapphire can in principle support wavelength into the deep UV; SiN has been shown to have significant optical absorption in wavelengths less than 470 nm and down into the UV range due to silicon incorporation into the layers inherent in the SiN growth [Karunagaran07]. Due to this, even though state-of-the-art SiN on SiO₂ has lower

Table 2. AlN platform results in literature.

	AlN on sapphire (this work)	AlN on SiO ₂ [8, 12]	SiN on SiO ₂ [26, 52]
Resonator Q factor	$Q = 24k$ (369.5 nm) $Q = 140k$ (638 nm)	$Q = 7k$ (410 nm) ^{a)} [53] $Q = 110k$ (774 nm) [8]	$Q = 4.4k$ (290 nm) ^{b)} [54]
Supporting wavelength	UV (~210 nm) to IR [12, 50, 51]	UV (~320 nm) to IR [8]	VIS (~470 nm) to IR [38]
Crystallinity	Crystalline	Polycrystalline (c-axis grown)	Stoichiometric
Active properties	electro-optic: $r_{33} = \sim 1$ pm/V piezoelectric: $d_{33} = \sim 5$ pm/V [51, 55, 56]		electro-optic: 8.31 fm/V [57]
Single mode WG loss	75 dB/cm (369.5 nm) ^{c)} 4.9 dB/cm (638 nm) ^{c)}	650 dB/cm (400 nm) [36] 6.4 dB/cm (774 nm) ^{c)}	< 1 dB/cm (532 nm) [58] 1.5 dB/cm (850 nm) [59]
Thermal properties (waveguide material)	$\kappa = 285$ W/m·K $dn/dT = 2.32 \times 10^{-5}/K$ [12]		$\kappa = 1.4$ W/m·K $dn/dT = 1.0 \times 10^{-5}/K$ [60]

a) AlN disk resonator on Si pedestal

b) Disk resonator

c) Loss estimated from resonator Q factor

single mode waveguide loss compared to AlN single mode waveguides in the visible wavelength, AlN photonics platforms have the capability to operate in the UV regime. Furthermore, AlN has a high piezoelectric coefficient and moderately high electro-optic coefficient compared to materials used in commercially available phase and amplitude modulators, allowing for active optical components. Finally, AlN's high thermal conductivity κ and small thermo-optic coefficient dn/dT allows devices to be less sensitive to temperature fluctuations, which is important for its many potential applications that require high-precision manipulation, routing, and read-out.

We have demonstrated a PIC platform based on the crystalline, wurtzite AlN on top of a sapphire substrate. Both AlN and sapphire are wide bandgap (6.015 eV [Feneberg10]) and 8.8 eV [French90]), respectively) and transparent from the UV to the mid-infrared [Xiong12, Majkic15, Majkic17]. We observe record-high quality factors exceeding 20,000 down to 369.5 nm, which corresponds to record-low propagation loss at 369.5 nm for active optical materials that have $\chi^{(2)}$ properties. The nonlinear, electro-optic, and piezo-electric properties of AlN make it a promising active material for controlling and connecting atomic and atom-like quantum memories, as well as for other applications such as UV spectroscopy and solar-blind communications.

Characterization and testing of the Quantum Photonics Processor (QPP) reviewed two design flaws that are currently being corrected in new designs and fabrication runs. These flaws were first

that many of the ground leads for the MZI's were tied directly together on the chip itself to reduce the number of ground pins (and wire bonds) required, which had the negative consequence of created ground loops in our circuits. The second flaw was that the optical input and output of the device are on opposite sides of the chip which meant that having two couplers double the work required to optically align the system. Consequently, this initial design decreased the stability of the system and increased the risk the chip and fibers might collide and cause damage. This later flaw pointed out the important practical role of packaging when it comes quantum integrated photonic devices. As a part of this project we contracted and coordinated with three companies to create a packaging solution for the current version of the QPP. This included a source of custom PCBs designed to cope with the large number of required wire bonds (over 200) in such a small area. This operation will hopefully be completed by the end of the 2018 and the packaged device can be tested at the AFRL in house lab in 2019.

In-house quantum frequency conversion (QFC) experiments were based on Difference Frequency Generation (DFG) in Lithium Niobate. To satisfy the momentum conservation we need a special material called Periodically Poled Lithium Niobate PPLN, which also allows for long crystals (3-4cm) which increase the interaction length and there for the efficiency of the conversion. The main difficulty in this version of DFG is that the polling period must be very narrow to satisfy the conservation of momentum constraint. In particular it must be $2.34\mu\text{m}$ per period. This is a difficult size to produce and is significantly smaller than what is used in industry. The main focus of these experiments were to attempt/perform the challenging QFC between UV (applicable to trapped ion transitions) to telecomm wavelengths. In the future, we anticipate in-house trapped ion experiments to incorporate a second ion species with output in the visible (e.g. 650nm) which will substantially increase the efficiency of QFC to telecomm wavelengths.

We achieved a great deal of success with our design, fabrication and testing of our dual MZI in which were able to separate the resulting generated biphotons from the pump source at two output ports. We measured a coincidence ratio of over 97%. The total measured coincidences of photons detected where both photons came out the drop port is over two orders of magnitude higher than all other even permutations. This is to be contrasted to a conventional double bus device with symmetric coupling which would only see 25% of detected photon pairs making their way out of the drop side. These results are a step towards efficient, pump filtered, pure sources on a SOI platform. Changing the way that we pump the device, (i.e. pumping on the add side of the ring) leads to photons which do not share spectral correlations. The verification of such a result is in the plans for future experiments entailing this ring source. Once verified, the device can be considered for experiments based on the "heralding" of single photons. It is vital that no spectral correlations exist within each generated photon pair otherwise the detection of one photon would lead to a mixed state on the other, destroying the assumption of pure states later in the experiment.

We authored a comprehensive tutorial and analysis of Spontaneous Parametric Down-Conversion, where among other results, we derived formulas for the absolute pair-generation rate in experiments utilizing degenerate, collinear SPDC. Subsequently, we also tested the validity of

these formulas with three different experiments. The first experiment tested the generation rate for type-0 SPDC in a periodically-poled bulk medium, of biphotons coupled into a single-mode optical fiber. The second experiment tested the generation rate for type-I SPDC in a bulk crystal, collected over all spatial modes. The third experiment tested the generation rate for type-II SPDC in a periodically poled single-mode nonlinear waveguide also coupled into single-mode optical fiber. Results of these experiments were shown to be in very close agreement to theoretical predictions.

The analysis of nonlinear optical processes in MMR lead to (i) the prediction of a much wider parameter space of HOMI (called HOMI manifolds) and (ii) a detailed study of biphoton generation within MRR. Currently, an integrated waveguide chip has been fabricated and is being tested and characterized for in-house experiments to test the HOMI manifold prediction in the presence of loss. Rates for coincidence to accidentals, heralding efficiency and biphoton production rates within a MRR were developed and experimentally verified (see previous practice), with very good agreement between theory and experiment.

In our study of the vertex cover problem for quantum annealers we encountered trouble embedding graphs with $d > 2$. For de Bruijn networks, we were able to find embeddings for the vertex cover problem with required/desired characteristics. We found that due to the chimera connectivity topology of the D-Wave systems architecture sparse graphs are needed. As the graphs grow chains of qubits are needed to recreate the connectivity needed and relatively quickly the graphs cannot be embedded into the machine. For future quantum algorithm research we are continuing to monitor as the D-Wave produces larger scale systems with the potential for better connectivity to see what problems (specifically Air Force relevant problems) can fit on the system. We are also beginning to research the new NISQ gate-based quantum processors, simulators and software. Our analysis will include how we program a gate-based quantum processor, do NISQ gate-based quantum processors provide a quantum advantage, what problems are they good at solving and what Air Force relevant problems could be solved on these processors.

6.0 REFERENCES

- [Alsing-Hach17a] P.M. Alsing, E.E. Hach III, C.C. Tison and A.M. Smith, "A quantum optical description of losses in ring resonators based on field operator transformations," Phys. Rev. A. 95, 053828 arXiv:1608.01280.
- [Alsing-Hach17b] P.M. Alsing and E.E. Hach III, "Photon-pair generation in a lossy micro-ring resonator. I. Theory," Phys. Rev. A 96, 033847 (2017); arXiv:1705.09227v2.
- [Alsing-Hach17c] P.M. Alsing and E.E. Hach III, "Photon-pair generation in a lossy micro-ring resonator. II. Entanglement in the output mixed Gaussian squeezed state," Phys. Rev. A Phys. Rev. 96, 033848 (2017); arXiv:1708.01338.
- [Aspar01] B. Aspar, H. Moriceau, E. Jalaguier, C. Lagahe, A. Soubie, B. Biasse, A. M. Papon, A. Claverie, J. Grisolia, G. Benassayag, F. Letertre, O. Rayssac, T. Barge, C. Maleville, and B. Ghyselen, "The Generic Nature of the Smart-Cut Process for Thin Film Transfer," J. Electron. Mater., 30, 834--840 (2001).
- [Bennink10] Bennink, Ryan S., "Optimal collinear Gaussian beams for spontaneous parametric down-conversion" Phys. Rev. A, 81, 053805 (2010).
- [Childress14] L. Childress, R. Walsworth, and M. Lukin, "Atom-like crystal defects: From quantum computers to biological sensors," Phys. Today (10), 38--43 (2014).
- [Dixon14] Dixon, P. B., et al., "Heralding Efficiency and correlated-mode coupling of near-IR fiber-coupled photon pairs", Phys. Rev. A, 90, 043804 (2014).
- [Duan10] L.-M. Duan and C. Monroe, "Quantum networks with trapped ions," Rev. Mod. Phys., 82, 1209--1224 (2010).
- [Dutt17] A. Dutt, "On-chip Quantum and Nonlinear Optics: From Squeezing to Spectroscopy," PhD Thesis (2017).
- [Fang94] S. P. Fang and H. F. Taylor, "High-performance single-mode fiber-optic switch," Opt. Lett., 19, 1204--1206 (1994).
- [Feneberg10] M. Feneberg, R. A. R. Leute, B. Neuschl, K. Thonke, and M. Bickermann, "High-excitation and high-resolution photoluminescence spectra of bulk AlN," PRB, 81, 075208 (2010).

[French90] R. H. French, "Electronic Band Structure of Al_2O_3 , with Comparison to AlOx and AlN ," J. Am. Ceram. Soc. (3), 477--489 (1990).

[Fujii77] Y. Fujii, S. Yoshida, S. Misawa, S. Maekawa, and T. Sakudo, "Nonlinear optical susceptibilities of AlN film," Appl. Phys. Lett., 815-816 (1977).

[Garey79] M.R. Garey and D.S. Johnson, "Computers and Intractability: Guide to the Theory of NP-Completeness," WH Freeman and Company, New York (1979).

[Goban14] A. Goban, C.-L. Hung, S.-P. Yu, J. D. Hood, J. A. Muniz, J. H. Lee, M. J. Martin, A. C. McClung, K. S. Choi, D. E. Chang, O. Painter, and H. J. Kimble, "Atom-light interactions in photonic crystals," Nat. Commun., 3808 (2014).

[Gorin08] A. Gorin, A. Jaouad, E. Grondin, V. Aimez, and P. Charette, "Fabrication of silicon nitride waveguides for visible-light using PECVD: a study of the effect of plasma frequency on optical properties," 13509--13516 (2008).

[Guo16] X. Guo, C.-L. Zou, H. Jung, and H. X. Tang, "On-Chip Strong Coupling and Efficient Frequency Conversion between Telecom and Visible Optical Modes," Phys. Rev. Lett. (12), 123902 (2016).

[Guo17] X. Guo, C.-L. Zou, C. Schuck, H. Jung, R. Cheng, and H. X. Tang, "Parametric down-conversion photon-pair source on a nanophotonic chip," Light Sci. Appl. (5), e16249 (2017).

[Harris15] N.C. Harris, et al, "Bosonic transport simulations in a large-scale programmable nanophotonic processor" arXiv:1507.03406 (2015)

[Harris17] N.C. Harris, et al., "Quantum Transport simulations in a programmable nanophotonic processor", Nature Photonics 11,447-452 (2017)

[Heck14] M. J. R. Heck, J. F. Bauters, M. L. Davenport, D. T. Spencer, and J. E. Bowers, "Ultra-low loss waveguide platform and its integration with silicon photonics," Laser Photonics Rev. (5), 667--686 (2014).

[Hoffman16] L. Hoffman, A. Subramanian, P. Helin, B. Du Bois, R. Baets, P. Van Dorpe, G. Gielen, R. Puer, and D. Braeken, "Low Loss CMOS-Compatible PECVD Silicon Nitride Waveguides and Grating Couplers for Blue Light Optogenetic Applications," IEEE Photon. J. (5), 2701211 (2016).

[Hong87] C.K Hong et. al, Measurement of subpicosecond time intervals between two photons by interference, Phys. Rev. Lett. 59, (1987).

[Ikeda08] K. Ikeda, R. E. Saperstein, N. Alic, and Y. Fainman, ``Thermal and Kerr nonlinear properties of plasma-deposited silicon nitride/ silicon dioxide waveguides," (17), 12987--12994 (2008).

[Jung13] H. Jung, C. Xiong, K. Y. Fong, X. Zhang, and H. X. Tang, ``Optical frequency comb generation from aluminum nitride micro-ring resonator," 2810--2813 (2013).

[Jung14] H. Jung, R. Stoll, X. Guo, D. Fischer, and H. X. Tang, ``Green, red, and IR frequency comb line generation from single IR pump in AlN micro-ring resonator," Optica, 396 (2014).

[Jung16] H. Jung and H. X. Tang, ``Aluminum nitride as nonlinear optical material for on-chip frequency comb generation and frequency conversion," Nanophotonics (2), 263--271 (2016).

[Karunagaran07] B. Karunagaran, S. J. Chung, S. Velumani, and E.-K. Suh, ``Effect of rapid thermal annealing on the properties of PECVD SiN thin films," Mater. Chem. Phys., 130--133 (2007).

[Kim13] J. Kim, R. Clark and D. Gauthier, ``Low-Noise Frequency Downconversion for Long-Distance Distribution of entangled Atomic Qubits" 2013 IEEE Photonics Society Summer Topical Meeting Series, pages 183-184, (2013).

[Krischeck10] R. Krischeck, W. Wieczorek, A. Ozawa, N. Kiesel, P. Michelberger, T. Udem, and H. Weinfurter, ``Ultraviolet enhancement cavity for ultrafast nonlinear optics and high-rate multiphoton entanglement experiments," Nat. Photonics (3), 170--173 (2010).

[Kurz18] C. Kurz, *et. al*, ``Programmable atom-photon quantum interface", Phys. Rev. A 93, 062348 (2016).

[Lee11] H. Lee, T. Chen, J. Li, O. Painter, and K. J. Vahala, ``Ultra-low-loss optical delay line on a silicon chip," Nat. Commun., 1-7 (2012).

[Levy09] J. S. Levy, A. Gondarenko, M. A. Foster, A. C. Turner-Foster, A. L. Gaeta, and M. Lipson, ``CMOS-compatible multiple wavelength oscillator for on-chip optical interconnects," Nat. Photonics (1), 37--40 (2010).

[Levy11] J. Levy, ``Integrated nonlinear optics in silicon nitride waveguides and resonators," PhD Thesis (2011).

- [Lin14] P. T. Lin, H. Jung, L. C. Kimerling, A. Agarwal, and H. X. Tang, "Low-loss aluminium nitride thin film for mid-infrared microphotonics," *Laser Photon. Rev.*, L23-L28 (2014).
- [Liu16] X. Liu, C. Sun, B. Xiong, L. Wang, J. Wang, Y. Han, Z. Hao, H. Li, Y. Luo, J. Yan, T. Wei, Y. Zhang, and J. Wang, "Broadband frequency comb generation in aluminum nitride-on-sapphire microresonators," *arXiv:1611.01994v2* (2016).
- [Liu17a] X. Liu, C. Sun, B. Xiong, L. Wang, J. Wang, Y. Han, Z. Hao, H. Li, Y. Luo, J. Yan, T. Wei, Y. Zhang, and J. Wang, "Aluminum nitride-on-sapphire platform for integrated high-Q microresonators," 587--594 (2017).
- [Liu17b] X. Liu, C. Sun, B. Xiong, L. Wang, J. Wang, Y. Han, Z. Hao, H. Li, Y. Luo, J. Yan, T. Wei, Y. Zhang, and J. Wang, "Integrated continuous-wave aluminum nitride Raman laser," *Optica*, 893--896 (2017).
- [Lueng00] C. M. Lueng, H. L. W. Chan, C. Surya, and C. L. Choy, "Piezoelectric coefficient of aluminum nitride and gallium nitride," *J. Appl. Phys.*, 5360-5363 (2000).
- [Majkic15] A. Majkic, U. Puc, A. Franke, R. Kirste, R. Collazo, Z. Sitar, and M. Zgonik, "Optical properties of aluminum nitride single crystals in the THz region," *Opt. Mater. Express*, 2106 (2015).
- [Majkic17] A. Majkic, U. Puc, A. Franke, R. Kirste, R. Schlessler, R. Collazo, Z. Sitar, and M. Zgonik, "Optical nonlinear and electro-optical coefficients in bulk aluminium nitride single crystals," *Phys. Status Solidi B*, 1700077 (2017).
- [Mehta16] K. K. Mehta, C. D. Bruzewicz, R. McConnell, R. J. Ram, J. M. Sage, and J. Chiaverini, "Integrated optical addressing of an ion qubit," *Nat. Nanotechnol.*, 1066 (2016).
- [Miller15] S. Miller, Y.-H. D. Lee, J. Cardenas, A. L. Gaeta, and M. Lipson, "Electro-optic effect in silicon nitride," in *CLEO* (2015), paper SF1G.4.
- [Miller17] S. A. Miller, M. Yu, X. Ji, A. G. Griffith, J. Cardenas, A. L. Gaeta, and M. Lipson, "Low-loss silicon platform for broadband mid-infrared photonics," *Optica*, 707--712 (2017).
- [Mikkelsen14] J. C. Mikkelsen, W. D. Sacher, and J. K. S. Poon, "Dimensional variation tolerant silicon-on-insulator directional couplers," 3145-3150 (2014).

- [Miyake16] H. Miyake, C. H. Lin, K. Tokoro, and K. Hiramatsu, "Preparation of high-quality AlN on sapphire by high-temperature face-to-face annealing," *J. Cryst. Growth*, 155--159 (2016).
- [Monroe13] C. Monroe and J. Kim, "Scaling the ion trap quantum processor," *Science*, 1164--1169 (2013).
- [Moss13] D. J. Moss, R. Morandotti, A. L. Gaeta, and M. Lipson, "New CMOS-compatible platforms based on silicon nitride and Hydex for nonlinear optics," *Nat. Photonics*, 597--607 (2013).
- [Mouradian15] S. L. Mouradian, T. Schroder, C. B. Poitras, L. Li, J. Goldstein, E. H. Chen, M. Walsh, J. Cardenas, M. L. Markham, D. J. Twitchen, M. Lipson, and D. Englund, "Scalable integration of long-lived quantum memories into a photonic circuit," *Phys. Rev. X*, 031009 (2015).
- [Mower15] J. Mower, N. C. Harris, G. R. Steinbrecher, Y. Lahini, and D. Englund, "High-fidelity quantum state evolution in imperfect photonic integrated circuits," *Phys. Rev. A*, 032322 (2015).
- [Muellner16] P. Muellner, A. Maese-Novo, E. Melnik, R. Hainberger, G. Koppitsch, J. Kraft, and G. Meinhardt, "CMOS-compatible low-loss silicon nitride waveguide integration platform for interferometric sensing," *ECIO* (2016).
- [Neel14] D. Neel, I. Roland, X. Checoury, M. El Kurdi, S. Sauvage, P. Boucaud, C. Brimont, T. Guillet, B. Gayral, and F. Semond, "AlN photonic crystals and microdisks for UV nanophotonics," *Adv. Nat. Sci: Nanosci. Nanotechnol.* 023001 (2014).
- [Nemoto14] K. Nemoto, M. Trupke, S. J. Devitt, A. M. Stephens, B. Scharfenberger, K. Buczak, T. N O'bauer, M. S. Everitt, J. Schmiedmayer, and W. J. Munro, "Photonic Architecture for Scalable Quantum Information Processing in Diamond," *Phys. Rev. X* (3), 031022 (2014).
- [Oh17] D. Y. Oh, K. Y. Yang, C. Fredrick, G. Ycas, S. A. Diddams, and K. J. Vahala, "Coherent ultra-violet to near-infrared generation in silica ridge waveguides," *Nat. Commun.*, 13922 (2017).
- [Pant17] M. Pant, H. Choi, S. Guha, and D. Englund, "Percolation based architecture for cluster state quantum computation using photon-mediated entanglement between atomic memories," *arXiv:1704.07292* (2017).

- [Pelc12] J.S. Pelc, *et al.* "Cascaded frequency upconversion for high-speed single-photon detection at 1550nm" *Optics Letters* vol 37 No 4 Feb 2012.
- [Pernice12] W. H. P. Pernice, C. Xiong, C. Schuck, and H. X. Tang, "Second harmonic generation in phase matched aluminum nitride waveguides and micro-ring resonators," *Appl. Phys. Lett.* (22), 223501 (2012).
- [Piazza06] G. Piazza, P. J. Stephanou, and A. P. Pisano, "Piezoelectric aluminum nitride vibrating contour-mode MEMS resonators," *J. Microelectromech. Syst.* (6), 1406--1418 (2006).
- [Poberaj09] G. Poberaj, R. Degl'Innocenti, C. Medrano, and P. Gunter, "UV integrated optics devices based on beta-barium borate," *Optical Materials*, 1049--1053 (2009).
- [Prabhu18] M. Prabhu, "Towards optimal capacity-achieving transceivers with photonic integrated circuits" <http://hdl.handle.net/1721.1/115725>.
- [Raymer-McKinstrie13] Raymer, M. and McKinstrie, C., "Quantum input-output theory for optical cavities with arbitrary coupling strength: application to two-photon wave-packet shaping," *Phys. Rev. A* 88, 043819 (2013).
- [Rutz16] H. Rutz, K.L. Luo, H. Suche and C. Silberhorn, "Quantum frequency conversion between infrared and ultraviolet," *Phys. Rev. Applied* 7, 024021 (2017).
- [Schneeloch18] J. Schneeloch, S.H. Knarr, D. F. Bogorin, M. L. Levangie, C. C. Tison, R. Frank, G. A. Howland, M. L. Fanto, and P. M. Alsing, "Introduction to the Absolute Brightness and number Statistics in Spontaneous Parametric Down-Conversion," *arXiv:quant-ph /1807.10885* (2018).
- [Schroeder73] J. Schroeder, R. Mohr, C. J. Montrose, and P. B. Macedo, "Light Scattering in a Number of Optical Grade Glasses," *J. Non-Cryst. Solids*, 313--320 (1980).
- [Selles16] J. Selles, C. Brimont, G. Cassabois, P. Valvin, T. Guillet, I. Roland, Y. Zeng, X. Checoury, P. Boucaud, M. Mexis, F. Semon, and B. Gayral, "Deep-UV nitride-on-silicon microdisk lasers," *Sci. Rep.*, 21650 (2016).
- [Soltani16] M. Soltani, R. Soref, T. Palacios, and D. Englund, "AlGaIn/AlN integrated photonics platform for the ultraviolet and visible spectral range," 25415 (2016).

- [Stegmaier14] M. Stegmaier, J. Ebert, J. M. Meckbach, K. Ilin, M. Siegel, and W. H. P. Pernice, ``Aluminum nitride nanophotonic circuits operating at ultraviolet wavelengths," *Appl. Phys. Lett.*, 091108 (2014).
- [Subramanian13] A. Z. Subramanian, P. Neutens, A. Dhakal, R. Jansen, T. Claes, X. Rottenberg, F. Peyskens, S. Selvaraja, P. Helin, B. Du Bois, K. Leyssens, S. Severi, P. Deshpande, R. Baets, and P. Van Dorpe, ``Low-loss singlemode PECVD silicon nitride photonic wire waveguides for 532-900 nm wavelength window fabricated within a CMOS pilot line," *IEEE Photon. J.* (6), 2202809 (2013).
- [Tison17] C. C. Tison, J. A. Steidle, M. L. Fanto, Z. Wang, N. A. Mogent, A. Rizzo, S. F. Preble, and P. M. Alsing, "Path to increasing the coincidence efficiency of integrated resonant photon sources," *Opt. Express* **25**, 33088-33096 (2017).
- [Togan10] E. Togan, Y. Chu, A. S. Trifonov, L. Jiang, J. Maze, L. Childress, M. V. G. Dutt, A. S. Sorensen, P. R. Hemmer, A. S. Zibrov, and M. D. Lukin, ``Quantum entanglement between an optical photon and a solid-state spin qubit," *Nature* (7307), 730--734 (2010).
- [Troha16] T. Troha, M. Rigler, D. Alden, I. Bryan, W. Guo, R. Kirste, S. Mita, M. D. Gerhold, R. Collazo, Z. Sitar, and M. Zgonik, ``UV second harmonic generation in AlN waveguides with modal phase matching," *Opt. Mater. Express* (6), 2014--2023 (2016).
- [Vernon17] Z. Vernon, M. Menotti, C. C. Tison, J. A. Steidle, M. L. Fanto, P. M. Thomas, S. F. Preble, A. M. Smith, P. M. Alsing, M. Liscidini, and J. E. Sipe, "Truly unentangled photon pairs without spectral filtering," *Opt. Lett.* 42, 3638-3641 (2017).
- [Xiong12a]] C. Xiong, W. H. P. Pernice, and H. X. Tang, ``Low-loss, Silicon Integrated, Aluminum Nitride Photonic Circuits and Their Use for Electro-Optic Signal Processing," *Nano Lett.* (7), 3562--3568 (2012).
- [Xiong12a] C. Xiong, W. H. P. Pernice, X. Sun, C. Schuck, K. Y. Fong, and H. X. Tang, ``Aluminum nitride as a new material for chip-scale optomechanics and nonlinear optics," *New J. Phys.*, 095014 (2012).
- [Xiong12b] C. Xiong, X. Sun, K. Y. Fong, and H. X. Tang, ``Integrated high frequency aluminum nitride optomechanical resonators," *Appl. Phys. Lett.*, 171111 (2012).
- [Walls94] D. Walls and G.J. Milburn, "Quantum Optics," Springer Verlag, NY, (1994).

[Yang07] J. K. W. Yang and K. K. Berggren, ``Using high-contrast salty development of hydrogen silsesquioxane for sub-10-nm half-pitch lithography," J. Vac. Sci. Technol. B (6), 2025 (2007).

[Yariv00] A. Yariv, ``Universal relations for coupling of optical power between microresonators and dielectric waveguides," Electronics Letters, 321--322 (2000).

[Yariv02] A. Yariv, ``Critical coupling and its control in optical waveguide-ring resonator systems," IEEE Photonics Technology Letters, 483--485 (2002).

7.0 LIST OF SYMBOLS, ABBREVIATIONS, AND ACRONYMS

AIM:	American Institute of Manufacturing
AlN:	aluminum nitride
AFM:	atomic force microscope
Ar:	argon
Ba:	barium
BCL:	boron trichloride
BOE:	buffered oxide etch
BS:	beam splitter
cm:	centimeter
cm ² /W:	centimeters squared/ watt
C:	Celsius
CAR:	coincidence to accidental rate
Cl:	chlorine
Cr:	Chromium
DBR:	distributed Bragg reflector
dB/cm:	decibel/centimeter
ECR:	electron cyclotron resonance
ECR-RIE:	electron cyclotron resonance reactive-ion etching
FWHM:	full width half maximum
FSR:	free spectral range
Gb/s:	gigabit/second
HF:	high frequency

HOMI:	Hong-Ou-Mandel Interference
HRXRD:	high resolution x-ray diffraction
HSQ:	hydrogen silsesquioxane
ICP-RIE:	inductively coupled plasma – reactive-ion etching
k:	thousand
keV:	kilo electron volt
LF:	low frequency
LN:	Lithium Niobate
MRR:	micro-ring resonator
mTorr:	millitorr
MZI:	Mach Zehnder Interferometer
N ₂ :	nitrogen
N ₂ O:	nitrous oxide
n:	index of refraction
n(g):	group index of refraction
NH ₃ :	ammonia
NaCl:	sodium chloride
NaOH:	sodium hydroxide
NISQ:	Noisy Intermediate-Scale Quantum
NP-Complete:	Nondeterministic polynomial time complete
NV:	nitrogen vacancy
nm:	nanometer
nm/min:	nanometer/minute
O:	oxygen
OAM:	Orbital Angular Momentum

OPO:	Optical Parametric Oscillation
OSA:	optical spectrum analyzer
PL:	photoluminescence
pm:	picometer
pm/V:	picometer/volt
PECVD:	plasma-enhanced chemical vapor deposition
PMMA:	Poly(methyl methacrylate)
PPKTP:	Periodically Poled Potassium Titanyl Phosphate
PPLN:	Periodically Poled Lithium Niobate
PVDNC:	plasma vapor deposition of nanocolumns
Q:	quality factor
QA:	Quantum annealing
QFC:	quantum frequency conversion
QPIC:	quantum photonic integrated circuit
Qubit:	Quantum bit
QUBO:	Quadratic Unconstrained Binary Optimization
RF:	radio frequency
RMS:	root mean squared
SEM:	scanning electron microscope
SiH ₄ :	silane
SiN:	silicon Nitride
SiO ₂ :	silicon dioxide
SiON:	silicon oxynitride
SFWM:	Spontaneous Four Wave Mixing
SFG:	Sum Frequency Generation

SHG:	Second Harmonic Generation
SM:	single mode
SNSPD:	Superconducting Nanowire Single Photon Detector
SOI:	silicon on insulator
SPDC:	Spontaneous Parametric Down Conversion
Sr:	strontium
TE:	transverse electric
Ti:Sapphire:	titanium doped sapphire
Yb:	ytterbium
um:	micrometer
UV:	ultraviolet
V:	Volts
VIS:	visible
W:	watts